PHYSICAL REVIEW FLUIDS **2**, 064603 (2017)

Hierarchy of antiparallel vortex tubes in spatially periodic turbulence at high Reynolds numbers

Susumu Goto,* Yuta Saito, and Genta Kawahara
Graduate School of Engineering Science, Osaka University, 1-3 Machikaneyama, Toyonaka, Osaka 560-8531, Japan
(Received 30 September 2016; published 6 June 2017)

To draw a precise picture of the hierarchy of coherent vortices in spatially periodic turbulence at high Reynolds numbers and to understand its generation mechanism, we conduct direct numerical simulations of turbulence in a periodic cube. By objectively identifying the axes of vortex tubes at various length scales in the inertial range, we quantitatively show that the sustained turbulence consists of a hierarchy of antiparallel pairs of vortex tubes. These vortex tubes are created by being stretched in strain fields around 2–8 times larger vortices, whereas they are weakened by strain around half-scale vortices. Temporal tracking of identified vortex tubes shows that they tend to form antiparallel pairs from the moment they are created. We examine three different external forces to show that the hierarchical structure of antiparallel vortex pairs is robust and its statistical features in inertial length scales are independent of the force. The turbulence that is sustained by steady forces is quasiperiodic in time and its significant temporal fluctuations are caused by successive creation of strong vortex tubes within the hierarchy.

DOI: 10.1103/PhysRevFluids.2.064603

I. INTRODUCTION

Richardson [1] explained the physics of relative dispersion of fluid particles in developed turbulence on the basis that turbulence is composed of a hierarchy of eddies with various sizes. As described in his famous verse [2], the energy is transferred within the hierarchy in a scale-by-scale manner and this energy cascade phenomenologically explains the origin of the small-scale universality of turbulence statistics. As predicted by Kolmogorov [3] and widely supported by experiments (see, e.g., Ref. [4]), the two-point velocity correlation function of turbulence at high Reynolds numbers obeys a power law for inertial length scales between the Kolmogorov length η and the integral length L. This implies that the hierarchy of flow structures is self-similar in a statistical sense. Therefore, an important problem in the study of turbulence is to draw a concrete picture of the self-similar hierarchy and to clarify its generation mechanism, i.e., the energy cascade dynamics.

Quite a few cascade models such as the log-normal model [5], the β model [6], the random β model [7], and the log-Poisson model [8] were proposed to describe the spatial intermittency [9]. For example, the well-known cartoons by Frisch *et al.* [6] depicted the notion of the energy cascade and origin of the intermittency. However, the cascade models do not explain the details of hierarchical flow structures or cascade dynamics.

Direct numerical simulations (DNSs) of turbulence in a periodic box have played an important role in the investigation of its flow structures and dynamics. In particular, the discovery of coherent intense vortices at the dissipative length scale [10–13] in numerically simulated turbulence significantly affected later research. It was also verified using DNSs that the energy evidently transfers from lower- to higher-wave-number Fourier modes on average [14–16]. However, the Reynolds numbers of these DNSs in the past century were not large enough to reveal the corresponding real-space physics of hierarchical flow structures. Among them, Hussain and co-workers pioneered this field

*goto@me.es.osaka-u.ac.jp.

of research on the basis of the notion of coherent structures [17] and developed cascade pictures by supplementing the smallness of the Reynolds number of their DNSs with the knowledge of vortex dynamics. In particular, the schematic in Fig. 19 of Ref. [18] conjectured a hierarchical structure of coherent vortices. As will be shown below, their concept that smaller-scale vortices are created in strain fields around larger-scale vortices is supported by our DNS.

A theoretical study by Lundgren [19] analytically derived a solution to the Navier-Stokes equations in the form of a spiral vortex that led to a power law of the velocity correlation function consistent with the Kolmogorov theory [3]. The Lundgren spiral and related pictures [20] are therefore candidates for the (statistically) self-similar flow structure in developed turbulence. Horiuti and co-workers [21,22] claimed that there are spiral vortices in their DNS turbulences. More recently, Kerr [23] also conducted DNSs with an organized initial condition to investigate a process leading to turbulence and compared the vortical structures observed in the DNSs with the Lundgren spiral. However, there is no numerical evidence to show the existence of the Lundgren spiral that spreads over many length scales and sustains the spatial velocity correlation in the entire inertial range predicted by the Kolmogorov theory.

About thirty years had passed since the pioneering study by Orszag and Patterson [24], when Kaneda *et al.* [25] conducted DNS of fully developed turbulence sufficiently beyond the so-called mixing transition [26], at which clear multiscale features of turbulence with a well-established scale separation (i.e., $L/\eta \gg 1$) emerge. Computational resources have now developed far enough to conduct sufficiently long-term DNSs of turbulence under simple boundary conditions at Reynolds numbers as high as those in the laboratory. Because DNSs possess all spatiotemporal information, they can help us to investigate the hierarchical structures and their dynamics in turbulence.

The first objective of this paper is to draw a concrete picture of the hierarchy of coherent vortical structures in spatially periodic turbulence using DNS at sufficiently high Reynolds numbers. In other words, we aim at quantitatively examining and improving the pictures suggested by previous authors (see, e.g., Refs. [11,17–19,21–23]; see also [27–29]), including ourselves [30,31]. However, to attain this objective, we are immediately faced with two problems. The first problem is how to extract such a hierarchy of flow structures in turbulence that has continuous length scales. Wavelets have been used [32], but this sophisticated tool has not yet led to a clear conclusion on the hierarchy. A method using a filter of the Fourier modes of velocity is, by contrast, naive but useful in practice (see, e.g., Ref. [33]). We also employ the latter simple method. The second problem is how to identify coherent vortices. The simplest way may be to use the isosurface of the coarse-grained enstrophy $\widehat{Q}$. In previous papers [30,31] we showed with visualizations of isosurfaces of $\widehat{Q}$, which was evaluated through Fourier mode filtering, that smaller-scale vortices were created in strain fields around larger-scale antiparallel (counterrotating) pairs of vortex tubes. However, in these previous studies we only observed a few examples of antiparallel pairs of vortex tubes and the statistical significance of such events was largely unknown. Furthermore, there is an inevitable problem in that the threshold of an isosurface may be chosen arbitrarily and one can look at only intense vortices in isosurface visualizations. As emphasized by Jiménez *et al.* [34], turbulence statistics are not sustained only by intense vortices; therefore, we need to objectively identify vortices with various strength (see a seminal study by Jeong and Hussain [35]). In this study, we use the so-called low-pressure method proposed by Miura and Kida [36,37]. This threshold-free method identifies the axis of a vortex tube using the fact that the pressure field takes a local minimum at the center of a vortex tube on the plane perpendicular to it. The method was originally proposed for identifying vortex tubes at the dissipative scale, but we apply it to coarse-grained pressure fields and identify vortex axes at any hierarchy level. Using this method, we will show in the following sections that vortex tubes at any inertial length scale indeed tend to form antiparallel pairs irrespective of the type of large-scale forces.

The second objective of this paper is to clarify the generation mechanism of the observed hierarchy of antiparallel pairs of vortex tubes. In our previous studies [30,31] we were only able to give two possibilities and we could not show which was the dominant mechanism. One possibility was the advection effect observed in the dynamics of vortex filaments [38] and the other was the mechanism

observed in the creation of small-scale vortices (threads) in larger-scale strain fields [18]. We have numerically tracked the identified coherent vortices and we will show in the following that the predominant mechanism of the formation of antiparallel vortex pairs is simultaneous or successive stretching of several smaller-scale vortex tubes in a single large-scale strain field rather than Siggia's mechanism [38] due to self- and mutually induced advection.

II. DIRECT NUMERICAL SIMULATION

We numerically integrated the Navier-Stokes equation for an incompressible fluid under periodic boundary conditions in all three orthogonal directions. The spatial period of the boundary condition is denoted by $\mathcal{L}$ $(=2\pi)$. We use the fourth-order Runge-Kutta-Gill scheme for the temporal integration. The spatial derivatives are evaluated using the Fourier spectral method. The aliasing errors are removed by the phase shift technique. The number N^3 of the Fourier modes was chosen depending on the Reynolds number so $k_{\max}\eta$ (with $k_{\max}$ being the largest resolved wave number) is always larger than unity throughout the DNS, even when the Kolmogorov length $\eta(t)$ $[=\epsilon(t)^{-1/4}\nu^{3/4}]$ fluctuates significantly in time (see Sec. III E). Here ν and $\epsilon(t)$ are the kinematic viscosity of the fluid and the energy dissipation rate per unit mass, respectively. We simulate fully developed turbulence where the average of the Reynolds number, based on the Taylor length (λ), $\langle R_\lambda\rangle = \langle u'\lambda/\nu\rangle \approx 750$ at the highest by using up to $N^3 = 2048^3$ modes. Here u' is defined by $u' = \sqrt{2K(t)/3}$, with $K(t)$ being the kinetic energy per unit mass, and angular brackets denote the temporal average. The integral length is evaluated by

$$L(t) = \frac{3\pi}{4K(t)} \int_0^\infty k^{-1} E(k,t) dk, \tag{1}$$

where $E(k,t)$ is the energy spectrum at wave number k. As will be shown in Sec. III E, the examined turbulence quasiperiodically evolves with significant fluctuations and its period is much longer than the turnover time $T = \langle L\rangle/\langle u'\rangle$ of the largest eddies. We therefore conduct each run of the DNS for a sufficiently long time, which is shortest $(18.8T)$ for the highest-Reynolds-number case, so that we can accurately evaluate the temporal averages.

We examine three different kinds of external forces to sustain turbulence in the periodic cube. One of them is a conventional but rather artificial force, which is denoted by $\boldsymbol{f}^{(R)}$. In this forcing scheme, we rescale and fix the magnitudes of the Fourier modes of the velocity for wave numbers smaller than $k_f = \sqrt{8}$ after each time step of the numerical integration of the unforced Navier-Stokes equation. Since the phases of these fixed modes evolve in time with a time scale of the order of the turnover time of the largest-scale eddies, large-scale flow structures freely move in space.

The other two forces are simple steady ones. Previous authors of studies of turbulence in a periodic cube preferred large-scale forces that made the turbulence as homogeneous, isotropic, and stationary as possible at length scales smaller than the integral length L. This is a reason why artificial forces such as $\boldsymbol{f}^{(R)}$ have been frequently used. However, it is not clear *a priori* the extent to which large-scale force affects smaller scales (see Sec. III D). Therefore, in the present study, we also use the well-defined steady forces

$$\boldsymbol{f}^{(V)} = \begin{bmatrix} -\sin(2\pi x/\mathcal{L})\cos(2\pi y/\mathcal{L}) \\ +\cos(2\pi x/\mathcal{L})\sin(2\pi y/\mathcal{L}) \\ 0 \end{bmatrix} \tag{2}$$

and

$$\boldsymbol{f}^{(K)} = \begin{bmatrix} \sin(2\pi y/\mathcal{L}) \\ 0 \\ 0 \end{bmatrix}, \tag{3}$$

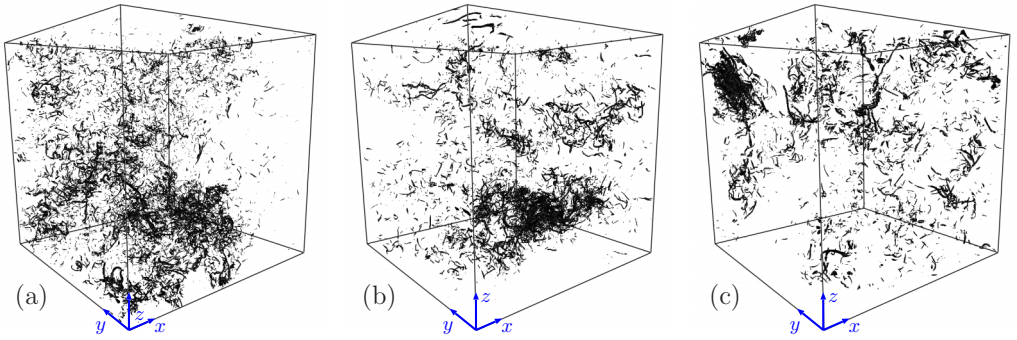

FIG. 1. Isosurfaces of the enstrophy of turbulence sustained by (a) $\boldsymbol{f}^{(R)}$ ($\langle R_\lambda \rangle = 390$), (b) $\boldsymbol{f}^{(V)}$ ($\langle R_\lambda \rangle = 480$), and (c) $\boldsymbol{f}^{(K)}$ ($\langle R_\lambda \rangle = 490$). The threshold is set as $m + 8\sigma$ with m and σ being the spatial mean and standard deviation of the enstrophy. The size of the shown cube is (a) $(\mathcal{L}/2)^3 \approx (3.5\langle L \rangle)^3 \approx (1500\langle \eta \rangle)^3$, (b) $(\mathcal{L}/2)^3 \approx (2.5\langle L \rangle)^3 \approx (1000\langle \eta \rangle)^3$, and (c) $(\mathcal{L}/2)^3 \approx (2.1\langle L \rangle)^3 \approx (1100\langle \eta \rangle)^3$.

at the cost of large-scale isotropy and homogeneity. The forcing wave number k_f is $\sqrt{2}$ and 1 for $\boldsymbol{f}^{(V)}$ and $\boldsymbol{f}^{(K)}$, respectively. The flow driven by $\boldsymbol{f}^{(K)}$ is called the Kolmogorov flow (see a review by Obukhov [39]) and the two-dimensional Kolmogorov flows have been extensively studied. Although this force was used for numerical simulations of three-dimensional turbulence in early periods [40], it has not been frequently used for the above-mentioned reason.

These time-independent forces $\boldsymbol{f}^{(V)}$ and $\boldsymbol{f}^{(K)}$ sustain a quadruplet of vortex tubes and a pair of vortex sheets in a periodic cube, respectively. In both cases, the steady flow $\boldsymbol{u} = \mathcal{L}^2/(4\pi^2\nu)\boldsymbol{f}$ is stable when ν is sufficiently large. For a smaller value of ν, we conduct DNSs of turbulence with an initial condition made by disturbing the steady flow. Since the pioneering study by Brachet *et al.* [41], such simple (so-called Taylor-Green) vortices expressed in terms of a few Fourier modes have been often used as an initial condition of the DNS of decaying turbulence, but in the present study we keep forcing.

For each of the DNSs with the three forces, sustained turbulence with a larger value of ν is used as the initial condition of the DNSs with smaller ν. In the following analysis, we will discard an initial transient period of the order of several turnover times of the largest-scale eddies.

III. RESULTS

A. Hierarchy of vortex tubes

We show the isosurfaces of the enstrophy field $Q(\boldsymbol{x},t) = |\boldsymbol{\omega}(\boldsymbol{x},t)|^2$ [i.e., the squared vorticity $\omega(\boldsymbol{x},t)$] driven by the three different large-scale forces $\boldsymbol{f}^{(R)}$, $\boldsymbol{f}^{(V)}$, and $\boldsymbol{f}^{(K)}$ in Fig. 1. In this figure, relatively strong vortices with enstrophy larger than $m(t) + 8\sigma(t)$, where $m(t)$ and $\sigma(t)$ are the spatial mean and standard deviation of $Q(\boldsymbol{x},t)$ at time t, respectively, are plotted. Despite the significant difference in the large-scale forces, there always exist wormlike structures and no qualitative difference in these structures is observed in the three panels in Fig. 1. This is qualitatively consistent with the small-scale universality because the enstrophy field is predominantly determined by the smallest-scale vortices.

Since the Reynolds numbers of the turbulences shown in Fig. 1 are high enough, they must be composed of a hierarchy of vortices with various sizes. However, it is difficult to recognize such a hierarchy by simply looking at the wormlike vortices. It is worth mentioning that a cluster of wormlike vortices does not necessarily correspond to a larger-scale vortex. See the Appendix for more detailed arguments on this point. In other words, to capture a hierarchy of vortices, we have to coarse grain the vorticity field $\boldsymbol{\omega}(\boldsymbol{x},t)$. As mentioned in Sec. I, we evaluate the coarse-grained

enstrophy $\widehat{Q}(\boldsymbol{x},t) = |\widehat{\boldsymbol{\omega}}(\boldsymbol{x},t)|^2$ with a sharp bandpass filter[1] of the Fourier modes of the velocity. More precisely, we retain the Fourier modes only in a spherical shell $[k_c/\sqrt{2}, \sqrt{2}k_c]$ in wave-number space and we call this bandpass filter the coarse grain at k_c because k_c is located at the center of the band in the logarithmic scale. We denote the corresponding coarse-grained scale $\mathcal{L}/k_c$ by ℓ_c. The reason why we choose the filter width as $[k_c/\sqrt{2}, \sqrt{2}k_c]$ is twofold. One is that, as will be shown in Sec. III D (see Fig. 9), twice larger scales most significantly contribute to the vortex stretching of a given scale. The other reason is that, due to the second-order nonlinearity of the governing equations, the interaction of Fourier modes at a given wave number produces Fourier modes at the twice larger wave number. We have verified that the shape of coarse-grained vortices is not significantly affected even if we use a smoother filter (e.g., the Gaussian filter) and we will discuss (in Sec. III B) the possibility that our conclusions shown below depend on the choice of the coarse-grain method. The effect of bandpass filtering on the shape of vortices was also investigated in detail by Leung *et al.* [33].

We show, in Fig. 2, isosurfaces of coarse-grained enstrophy $\widehat{Q}(\boldsymbol{x},t)$ at different length scales for each of the three forces $\boldsymbol{f}^{(R)}$, $\boldsymbol{f}^{(V)}$, and $\boldsymbol{f}^{(K)}$. Note that even the blue fine vortices [Figs. 2(a iii)–2(c iii)] are at the hierarchy level of sufficiently large length scale in the inertial range corresponding to about (a) $66\langle\eta\rangle$, (b) $100\langle\eta\rangle$, and (c) $97\langle\eta\rangle$. Since the distribution of the coarse-grained enstrophy is more intermittent for smaller scales, we set the threshold of the isosurfaces larger ($\langle\widehat{m}\rangle + 3\langle\widehat{\sigma}\rangle$) in Figs. 2(a iii)–2(c iii) than $\langle\widehat{m}\rangle + 2\langle\widehat{\sigma}\rangle$ in Figs. 2(a i)–2(c i) and 2(a ii)–2(c ii). Here $\widehat{m}(t)$ and $\widehat{\sigma}(t)$ are the mean and the standard deviation, respectively, of $\widehat{Q}(\boldsymbol{x},t)$.

As shown in Figs. 2(a i)–2(c i), the shape of largest-scale vortices depends on the type of forcing. However, for shorter length scales (i.e., length scales shorter than about a quarter of the forcing scale), the coarse-grained vortices identified by the present method always look tubular irrespective of the type of external forces [Figs. 2(a ii)–2(c ii) and 2(a iii)–2(c iii)]. More precisely, vortices at smaller scales are tubelike with smaller radii and shorter lengths. Although many blue vortices look bloblike in Figs. 2(a iii)–2(c iii), they are actually tubular in magnified views (see Figs. 4 and 5 below).

Incidentally, it is trivial that the red vortices for $k_c = k_f$ in Fig. 2(b i) are tubular because they are directly driven by $\boldsymbol{f}^{(V)}$, which is defined by (2). It is interesting to observe that the red vortices in Fig. 2(c i) directly driven by $\boldsymbol{f}^{(K)}$ also look tubular in our visualization of the coarse-grained enstrophy with sharp bandpass Fourier filtering, although the force $\boldsymbol{f}^{(K)}$, defined by (3), is likely to sustain a pair of vortex sheets in a periodic cube.

In summary, the first conclusion drawn from our DNS is that spatially periodic turbulence, in the inertial length scales, is composed of a hierarchy of vortex tubes with different sizes.

B. Generation mechanism of vortex tubes at each hierarchy level

In this section we investigate the generation mechanism of vortex tubes at each level of the hierarchy on the basis of flow visualizations. Quantitative arguments are developed later in Secs. III C and III D.

Let us first examine vortex tubes at two relatively large length scales ($k_c = k_f$ and $4k_f$) in turbulence driven by $\boldsymbol{f}^{(V)}$. We show isosurfaces of coarse-grained enstrophy at these two length scales in Fig. 3. It is evident in Fig. 3(a) that yellow vortex tubes are perpendicular to the red ones and a conclusion immediately drawn from these visualizations is that vortex tubes at the hierarchy level ($k_c = 4k_f$) are created by being stretched in larger-scale ($k_c = k_f$) strain fields. This is clearly demonstrated in Fig. 3(b), which shows the creation process of yellow vortex tubes (at $k_c = 4k_f$) around red tubes (at $k_c = k_f$). The yellow vortices are concentrated in strong straining regions at

[1] In Refs. [30,31] we used a low-pass filter. Long thin vortices are frequently observed in the vorticity field low-pass filtered at a large wave number, but they are actually identical to those at larger scales. Low-pass filters are therefore inappropriate for identifying the hierarchy of vortices.

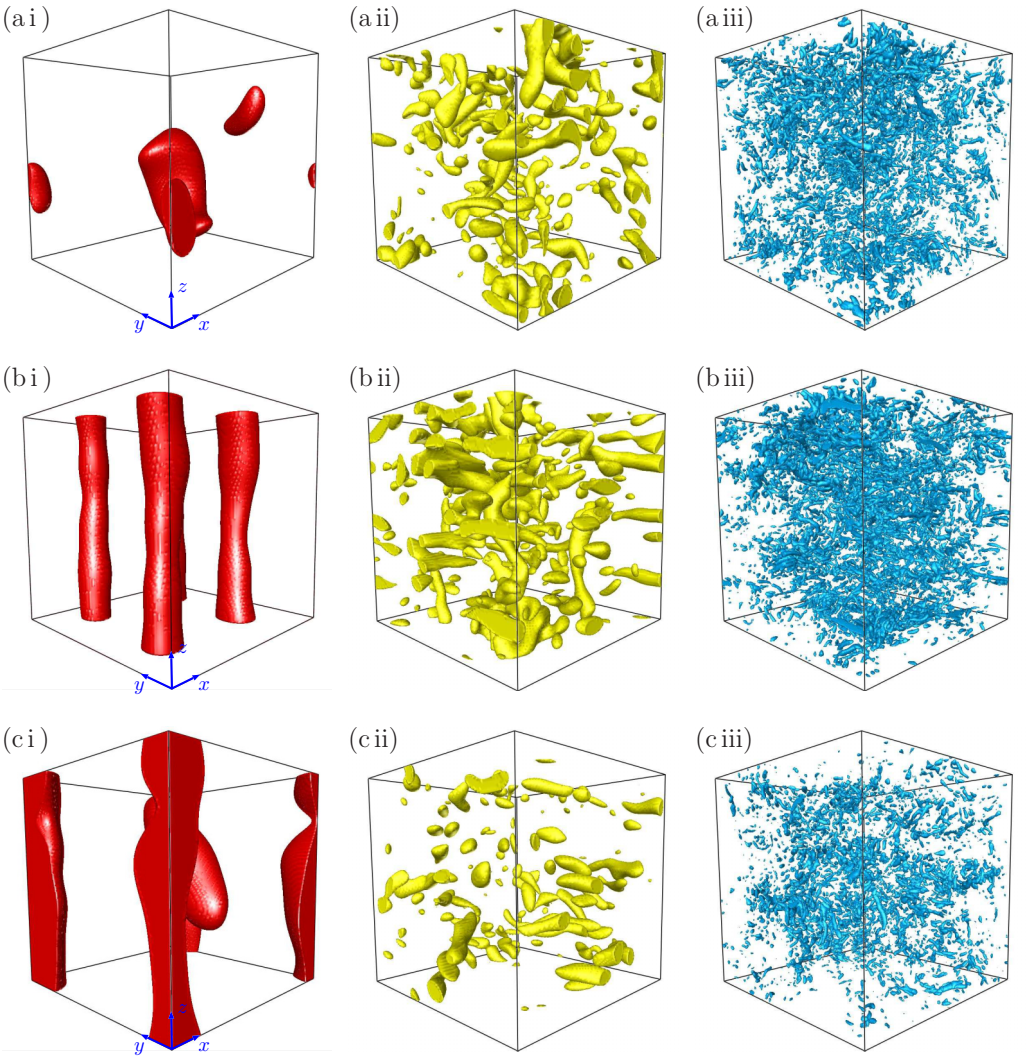

FIG. 2. Isosurfaces of the coarse-grained enstrophy in the turbulence driven by (a) $\boldsymbol{f}^{(R)}$, (b) $\boldsymbol{f}^{(V)}$, and (c) $\boldsymbol{f}^{(K)}$. The coarse-grained wave number is (a i) and (b i) $k_c = k_f$ and (c i) $k_c = \sqrt{2}k_f$, (a ii) and (b ii) $k_c = 4k_f$ and (c ii) $k_c = 4\sqrt{2}k_f$, and (a iii) and (b iii) $k_c = 16k_f$ and (c iii) $k_c = 16\sqrt{2}k_f$. The threshold of the isosurface is set at (i) and (ii) $\langle\widehat{m}\rangle + 2\langle\widehat{\sigma}\rangle$ and (iii) $\langle\widehat{m}\rangle + 3\langle\widehat{\sigma}\rangle$. The shown domain is the same as in Fig. 1 at the time (b) $t = 3.3T$ and (c) $t = 1.6T$ in Fig. 12.

$k_c = k_f$ around the quadruplet of the red tubes and they align along the stretching direction of the strain field at $k_c = k_f$.

Because the vortices and strain fields at $k_c = k_f$ are directly created by the external force $\boldsymbol{f}^{(V)}$, the above results [Figs. 3(a) and 3(b)] may be expected beforehand. However, an unexpected observation is found in Fig. 3(c), which shows a cropped part of the left middle region of Fig. 3(b). Looking at the coarse-grained velocity on a cross section of the created (yellow) vortex tubes, we notice that the vortex tubes tend to align in an antiparallel manner (i.e., their axes are parallel and their circulations are in opposite directions). Although details of the shape of vortices depend on the coarse-grain method, the appearance of antiparallel pairs of vortex tubes is unlikely to be an artifact of our method. In fact, we observed [30,31] antiparallel pairs of vortex tubes in the coarse-grained

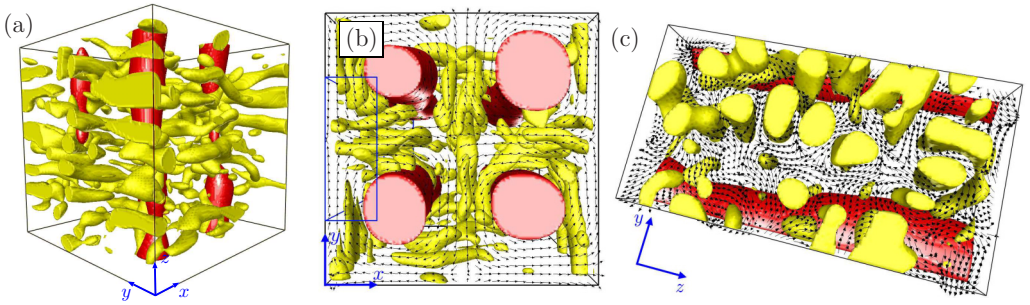

FIG. 3. (a) Isosurfaces of coarse-grained enstrophy (red, $k_c = k_f$; yellow, $4k_f$) with threshold $\langle \widehat{m} \rangle + 2\langle \widehat{\sigma} \rangle$ in the turbulence driven by $\boldsymbol{f}^{(V)}$. The box size is $\mathcal{L}^3 \approx (5.4\langle L \rangle)^3 \approx (2200\langle \eta \rangle)^3$. (b) Same as (a), but from a different line of sight. Arrows are the coarse-grained velocity at $k_c = k_f$. (c) View from another angle of a cropped region, shown with a blue frame, of the left center part of (b). Arrows are the coarse-grained velocity at $k_c = 4k_f$.

fields obtained by using low-pass filters, which have a much broader filter width than the bandpass filters. In addition, employing a sophisticated method (Ref. [42], for example), we may identify vortex sheets around individual vortex tubes (as demonstrated in Ref. [43] for Kolmogorov-scale vortices in high-resolution DNSs), but a pair of antiparallel vortex tubes would not be expressed as a single vortex sheet because they have opposite sign of the coarse-grained vorticity. We will discuss the generation mechanism of antiparallel pairs of vortices in Sec. III F.

The antiparallel pairs of vortex tubes at the quarter of the forcing length scale (i.e., $k_c = 4k_f$, yellow vortex tubes in Fig. 3), which are created in strain fields around the largest-scale vortices, also induce strong strain fields around themselves. Therefore, the creation events of further smaller vortex tubes are easily found around them. Figure 4(a) is a magnified view around a pair of yellow ($k_c = 4k_f$) vortex tubes in Fig. 3(a). We plot in Fig. 4(c) coarse-grained vorticity vectors in these yellow vortex tubes to verify that they form an antiparallel pair. Figure 4(a) shows that blue vortex tubes (at $k_c = 16k_f$) are created by being stretched in the strain field around the antiparallel pair of yellow tubes, and therefore that they are perpendicular to the pair. Furthermore, Figs. 4(b) and 4(d), which are further magnifications of Figs. 4(a) and 4(c), show that an antiparallel pair of the blue vortex tubes stretches and creates further smaller-scale (at $k_c = 64k_f$ corresponding to $\mathcal{L}/k_c \approx 25\langle \eta \rangle$) green vortex tubes. These are clear examples of the perpendicular alignment of vortices at different scales. However, because vortex tubes at a given scale are stretched simultaneously in strain fields at larger (more precisely, 2–8 times larger) scales (see Sec. III D), the alignment of fine vortex tubes is generally complicated and small-scale vortex tubes are not always aligned perpendicular to nearby twice-larger tubes, for example. We will return to this point in Sec. III D, where we show that strongly stretched vortices are indeed aligned in the perpendicular direction to larger-scale vortex tubes with strong vorticity.

Since the largest-scale vortex tubes driven by $\boldsymbol{f}^{(V)}$ are spatially fixed, we may easily recognize the hierarchical structure of vortex tubes in the turbulence sustained by $\boldsymbol{f}^{(V)}$. However, we emphasize that the tendency of antiparallel alignment of vortex tubes at each hierarchy level is never prescribed by the force. Indeed, such alignments are observed even at length scales much smaller than the forcing scale (Fig. 4). Furthermore, antiparallel pairs of vortex tubes are ubiquitous in turbulence driven by other forces. Examples are given in Fig. 5 for the other two forces $\boldsymbol{f}^{(R)}$ and $\boldsymbol{f}^{(K)}$. In addition to these observations, we will show statistical evidence of the tendency in Sec. III C.

We emphasize again that the hierarchy is created by vortex stretching. This process seems quite different from vortex breakups, which are the words sometimes used in an explanation of the energy cascade. Smaller vortices are created around, rather than inside, larger vortices. In this sense, the picture suggested by Hussain and co-workers [17,18] is supported by our DNSs. Our finding is that

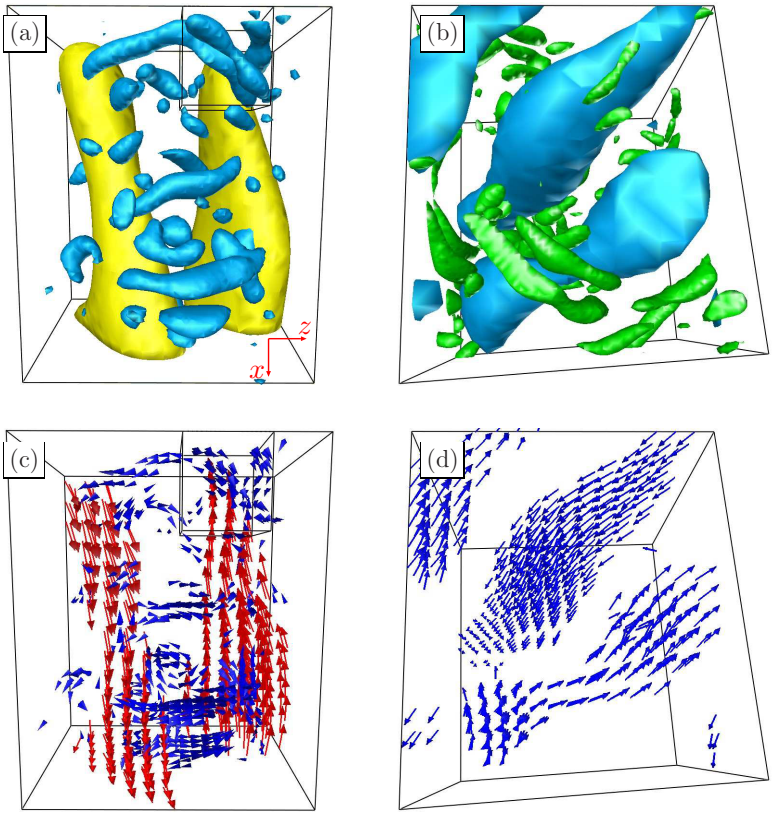

FIG. 4. Antiparallel pairs of small-scale vortex tubes and the creation of further smaller-scale levels of the hierarchy. (a) Isosurfaces of coarse-grained enstrophy (yellow, $k_c = 4k_f$; blue, $16k_f$). Magnified view of a part of Fig. 14(c), which is at a later time of Fig. 3(a), but with the threshold for the yellow isosurfaces reset as $\langle\widehat{m}\rangle + 4\langle\widehat{\sigma}\rangle$. The box size is $1.4\langle L\rangle \times 0.87\langle L\rangle \times 1.1\langle L\rangle \approx 560\langle\eta\rangle \times 360\langle\eta\rangle \times 450\langle\eta\rangle$. (b) Magnified view of the cropped part of (a) in a right top region. The box size is $0.33\langle L\rangle \times 0.37\langle L\rangle \times 0.31\langle L\rangle \approx 140\langle\eta\rangle \times 150\langle\eta\rangle \times 130\langle\eta\rangle$. Green blobs are isosurfaces of coarse-grained enstrophy at $k_c = 64k_f$ with threshold $\langle\widehat{m}\rangle + 8\langle\widehat{\sigma}\rangle$. (c) and (d) Coarse-grained vorticity vectors in the isosurfaces. The yellow vortex tubes in (a) and blue tubes in (b) form antiparallel pairs. Only the vectors for $k_c = 16k_f$ are plotted in (d) for visibility.

not a single vortex tube but pairs of them effectively stretch and create smaller-scale vortices at each hierarchical level.

C. Quantitative evidence of the antiparallel alignment of vortex tubes

We have only looked at strong vortices in the visualizations in the preceding sections. Let us show in this section that weaker vortex tubes also tend to form antiparallel pairs. For this purpose, we identify the axes of vortex tubes at each hierarchy level using the low-pressure method [36,37] and examine the angular distribution between them. More precisely, we first coarse grain the velocity field and then solve the Poisson equation to obtain the coarse-grained pressure field, to which we apply the low-pressure method. We visualize the identified vortex axes in turbulence driven by $\boldsymbol{f}^{(V)}$ in Figs. 6(a) and 6(b), which correspond to Figs. 3(a) and 4(a), respectively. The axes of both strong and weaker vortices are well identified at any level of the hierarchy. Comparing these figures, in particular, looking at the strong vortices identified both by the isosurface (Fig. 3) and by vortex axes (Fig. 6), we may confirm that our identification of the axis of coarse-grained vortices works very well. This is not trivial because we may obtain a coarse-grained pressure field by directly bandpass

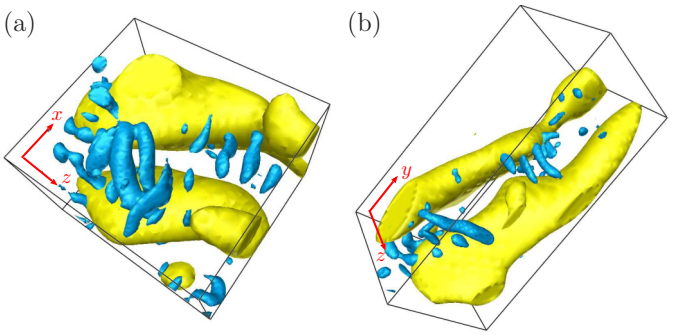

FIG. 5. Antiparallel pairs of small-scale vortex tubes in turbulence driven by (a) $\boldsymbol{f}^{(R)}$ and (b) $\boldsymbol{f}^{(K)}$. These figures are magnified views of Figs. 2(a ii) and 2(c ii), respectively, but the threshold is reset at $\langle\widehat{m}\rangle + \langle\widehat{\sigma}\rangle$. Blue blobs are isosurfaces (with the threshold being $\langle\widehat{m}\rangle + 4\langle\widehat{\sigma}\rangle$) of the coarse-grained enstrophy at the quarter length scale of the yellow vortices. The shown domain size is (a) $0.52\langle L\rangle \times 0.75\langle L\rangle \times 0.84\langle L\rangle \approx 220\langle\eta\rangle \times 310\langle\eta\rangle \times 350\langle\eta\rangle$ and (b) $0.40\langle L\rangle \times 0.44\langle L\rangle \times 0.89\langle L\rangle \approx 210\langle\eta\rangle \times 230\langle\eta\rangle \times 460\langle\eta\rangle$.

filtering the pressure field instead of solving the Poisson equation with the coarse-grained velocity field. We have compared the results of the two filtering methods and realized that the present method is better at capturing details of the coarse-grained vortical structures. The direct pressure filtering leads to a lower number of identified vortex axes, which are straight and different from the curved axes shown in Fig. 6. This is because the vorticity reconstructed from the directly filtered pressure is quite different from the coarse-grained vorticity, which is the target of the present analysis.

To quantitatively verify the tendency of the formation of antiparallel pairs, we evaluate the probability density function (PDF) of the cosine of the angle θ between the axes at a given coarse-grained scale. The PDF $P(\cos\theta|r)$ is conditioned by the distance r between them. More precisely, we divide each vortex axis into short segments of lengths of the order of the grid width and define the distance r and the angle θ of each pair of the segments only in the space between the two parallel planes (S_1 and S_2 in Fig. 7) that are perpendicular to one (the red one in Fig. 7) of the two segments at its end points. Then θ is defined as in Fig. 7, while r is estimated by the distance between the midpoints of the two segments.

The results are plotted in Fig. 8 for the three cases of different external forces. This figure clearly shows the tendency to form antiparallel pairs (i.e., $\cos\theta = -1$) of the vortex axes in a near region

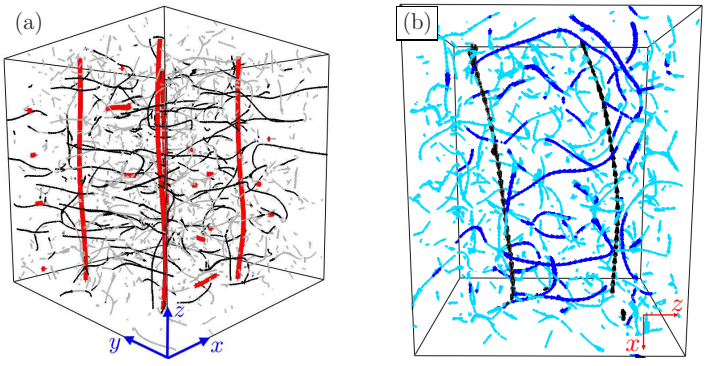

FIG. 6. Vortex axes identified using the low-pressure method. (a) Same field as in Fig. 3(a): red, axes of vortex tubes at $k_c = k_f$; black, stronger ($\widehat{Q} > \langle\widehat{m}\rangle + 2\langle\widehat{\sigma}\rangle$) vortex tubes at $k_c = 4k_f$; gray, weaker vortices at $k_c = 4k_f$. (b) Same field as in Fig. 4(b): black, axes of vortex tubes at $k_c = 4k_f$; blue, stronger ($\widehat{Q} > \langle\widehat{m}\rangle + 4\langle\widehat{\sigma}\rangle$) vortex tubes at $k_c = 16k_f$; light blue, weaker vortex tubes at $k_c = 16k_f$.

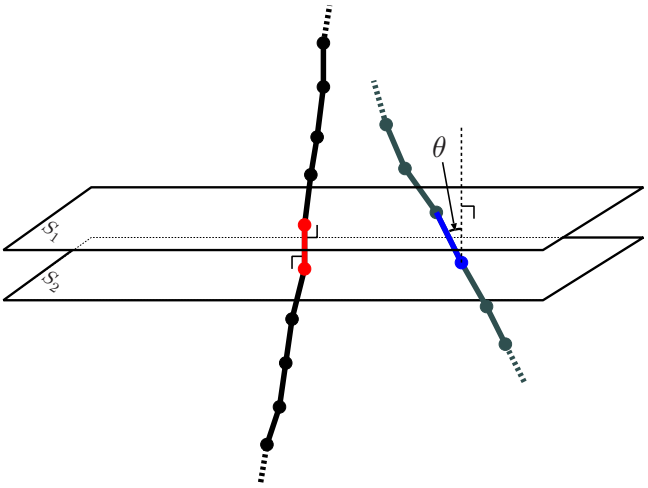

FIG. 7. Definition of the angle θ between two vortex axis segments.

$0.5\ell_c < r < 0.75\ell_c$, with ℓ_c being the coarse-grained scale $\mathcal{L}/k_c$. It must be emphasized that this antiparallel tendency of vortices is independent of the external force. Comparing the three panels in Fig. 8, it is noticeable that the PDF is almost identical for the three kinds of the forces.

This result not only supports the observation in the previous section, but also indicates that even weaker vortex tubes tend to align in an antiparallel manner. Incidentally, in the three-times-longer distance ($\ell_c < r < 1.5\ell_c$), $P(\cos\theta)$ is a constant ($\approx 1/2$), implying an isotropic distribution.

The second important observation in Fig. 8 is that the PDF is surprisingly independent of the coarse-grained scale. Note that the PDF of angles between vortex tubes at different coarse-grained wave numbers k_c are plotted with different colors in Fig. 8. This observation implies a self-similarity of the hierarchy of vortex tubes. Consistently, we have also verified that the PDF is independent of $\langle R_\lambda \rangle$ (figure is omitted).

To summarize this and the preceding section, the second conclusion of the present paper is that, at each hierarchy level, vortex tubes tend to form antiparallel pairs and they effectively stretch and create smaller-scale vortex tubes in strain fields around them. This conclusion is drawn not only from the visualizations (Figs. 3–5) but also from the statistics of the angle between vortex tubes (Fig. 8).

D. Scale locality of the stretching

In Sec. III B we have seen that smaller-scale vortex tubes at a hierarchy level are generated by being stretched in larger-scale strain field. It is therefore important to examine whether or not this stretching process is local in scale because it is the scale locality of the energy cascade that forms the basis of the universality of small-scale statistics. In this section we investigate the scale dependence of those factors that contribute to the stretching. Similar to the coarse-grained vorticity $\widehat{\omega}_i(k_c^{(\omega)})$, we define the coarse-grained strain tensor $\widehat{s}_{ij}(k_c^{(s)})$ using the bandpass filter in a wave-number range $[k_c^{(s)}/\sqrt{2}, \sqrt{2}k_c^{(s)}]$. Then the scale-dependent contributions to the stretching are evaluated using the following quantity:

$$G\left(k_c^{(s)},k_c^{(\omega)}\right) = \left\langle \frac{\overline{\widehat{\omega}_i\left(k_c^{(\omega)}\right)\widehat{s}_{ij}\left(k_c^{(s)}\right)\widehat{\omega}_j\left(k_c^{(\omega)}\right)}}{\left|\widehat{\boldsymbol{\omega}}\left(k_c^{(\omega)}\right)\right|^2} \right\rangle = \left\langle \overline{g\left(k_c^{(s)},k_c^{(\omega)}\right)} \right\rangle. \tag{4}$$

Here the overbar denotes the spatial average and $G(k_c^{(s)},k_c^{(\omega)})$ indicates the contribution to the stretching of coarse-grained vortices at $k_c^{(\omega)}$ from coarse-grained strain at $k_c^{(s)}$. Note that positive and

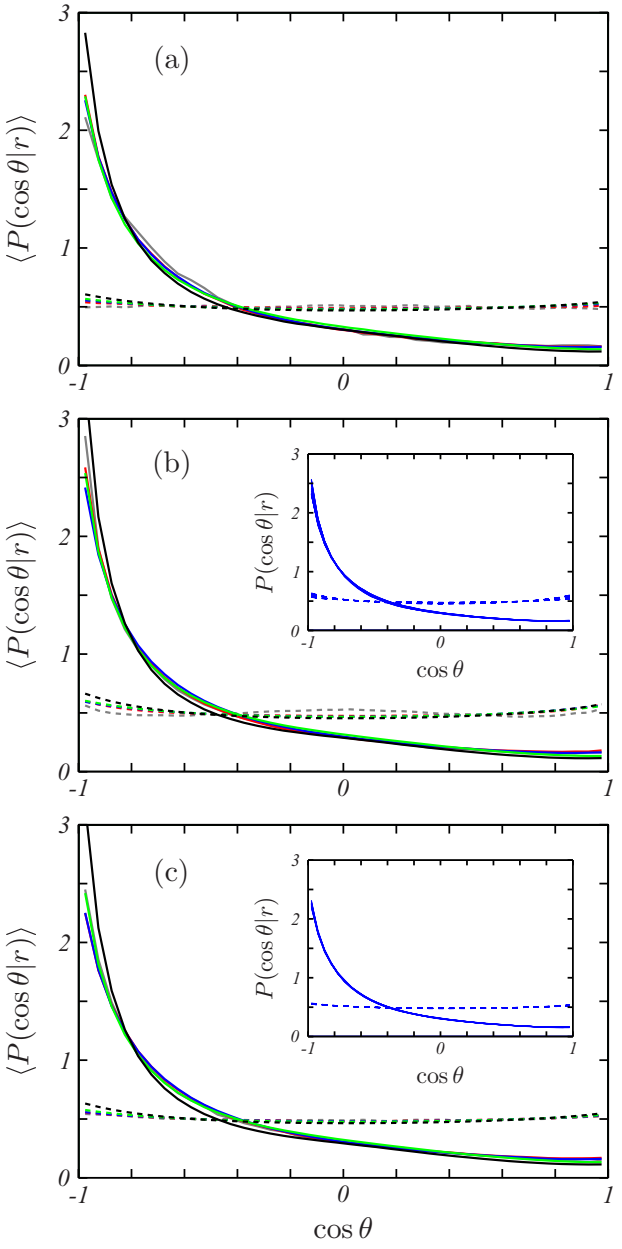

FIG. 8. (a) PDF of the cosine of the angle between vortex axes conditioned by their distance r: solid lines, $0.5\ell_c < r < 0.75\ell_c$; dotted, $1.5\ell_c < r < 2.25\ell_c$. Here ℓ_c $(= \mathcal{L}/k_c)$ is the coarse-grained length scale. Results are for the turbulence ($\langle R_\lambda\rangle = 390$) driven by $\boldsymbol{f}^{(R)}$. Different colors correspond to different coarse-grained scales: gray, $k_c = 2k_f$; red, $4k_f$; blue, $8k_f$; green, $16k_f$; black, $32k_f$. The temporally averaged values are plotted. (b) Results for the turbulence ($\langle R_\lambda\rangle = 480$) driven by $\boldsymbol{f}^{(V)}$. The temporal average for the coarse-grained scales at $k_c = 4k_f$ (gray), $8k_f$ (red), $16k_f$ (blue), $32k_f$ (green), and $64k_f$ (black). The inset shows the PDF for $k_c = 16k_f$ at 20 equidistant times along the black trajectory in Fig. 12(a) (see Sec. III E). (c) PDF for the turbulent Kolmogorov flow ($\langle R_\lambda\rangle = 490$) driven by $\boldsymbol{f}^{(K)}$. The temporal average for the coarse-grained scales at $k_c = 4\sqrt{2}k_f$ (gray), $8\sqrt{2}k_f$ (red), $16\sqrt{2}k_f$ (blue), $32\sqrt{2}k_f$ (green), and $64\sqrt{2}k_f$ (black). The inset shows the PDF for $k_c = 16\sqrt{2}k_f$ at 20 equidistant times along the trajectory in Fig. 12(b) (see Sec. III E).

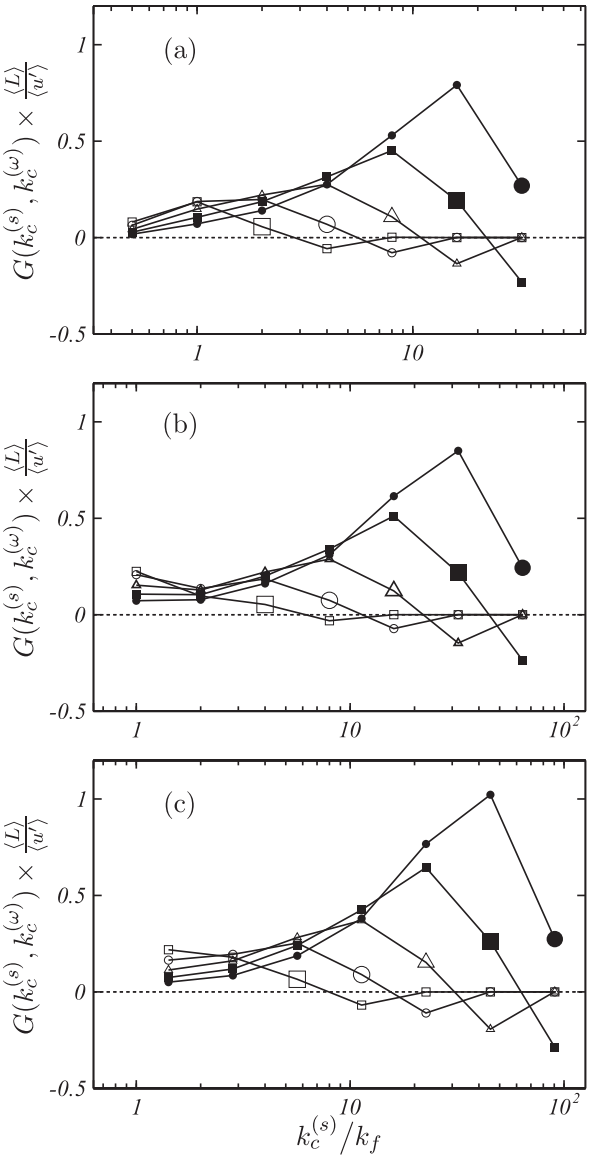

FIG. 9. (a) Contribution of the coarse-grained strain at $k_c^{(s)}$ to the stretching of coarse-grained vortices at $k_c^{(\omega)} = 2k_f$ (□), $4k_f$, (○), $8k_f$, (△), $16k_f$, (■), and $32k_f$ (●) in the turbulence ($\langle R_\lambda \rangle = 390$) driven by $\boldsymbol{f}^{(R)}$. The larger symbols correspond to self-contribution ($k_c^{(s)} = k_c^{(\omega)}$). (b) Same as (a) but for the turbulence ($\langle R_\lambda \rangle = 480$) driven by $\boldsymbol{f}^{(V)}$ at $k_c^{(\omega)} = 4k_f$ (□), $8k_f$ (○), $16k_f$ (△), $32k_f$ (■), $64k_f$ (●), and $128k_f$ (▲) (c) Same as (a) but for the turbulence ($\langle R_\lambda \rangle = 490$) driven by $\boldsymbol{f}^{(K)}$ at $k_c^{(\omega)} = 4\sqrt{2}k_f$ (□), $8\sqrt{2}k_f$ (○), $16\sqrt{2}k_f$ (△), $32\sqrt{2}k_f$ (■), and $64\sqrt{2}k_f$ (●).

negative values of G correspond to the stretch and contraction of the vortices, respectively. Results are plotted in Fig. 9 for the three different external forces: $\boldsymbol{f}^{(R)}$, $\boldsymbol{f}^{(V)}$, and $\boldsymbol{f}^{(K)}$. The important conclusion drawn from this figure is that the strain at the scale that is twice as large as the stretched vortices contributes most to the stretching. We emphasize that this tendency is independent of both the scale and the kind of the external force. It is also important that the feature is independent of the Reynolds number as shown in Fig. 10(a), in which three curves for three different Reynolds numbers collapse.

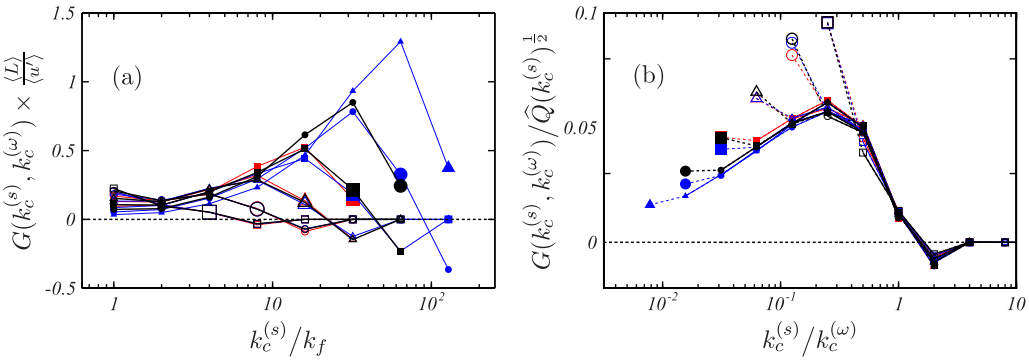

FIG. 10. (a) Same quantity as in Fig. 9 plotted for the turbulence driven by $\boldsymbol{f}^{(V)}$ at three different Reynolds numbers: $\langle R_\lambda\rangle = 280$ (red), 480 (black), and 750 (blue). The larger symbols correspond to self-contribution ($k_c^{(s)} = k_c^{(\omega)}$). (b) Same as (a), but with G and $k_c^{(s)}$ normalized by $\widehat{Q}(k_c^{(s)})^{1/2}$ and $k_c^{(\omega)}$, respectively. The larger symbols correspond to $k_c^{(s)} = k_f$.

In a related study, Leung *et al.* [33] showed that $\widehat{\omega}_i(k_c^{(\omega)})$ tends to align with the eigenvector of $\widehat{s}_{ij}(k_c^{(s)})$ with the largest eigenvalue at 3–5 times larger scales than the scale ($\sim\mathcal{L}/k_c^{(\omega)}$) of vorticity $\widehat{\omega}_i(k_c^{(\omega)})$. This trend is verified by normalizing $G(k_c^{(s)},k_c^{(\omega)})$ using the square root of the coarse-grained enstrophy $\widehat{Q}(k_c^{(s)})$ [Fig. 10(b)]. This figure implies that, except for $k_c^{(s)} = k_f$, the alignment between $\widehat{\omega}_i(k_c^{(\omega)})$ and the eigenvectors of $\widehat{s}_{ij}(k_c^{(s)})$ is self-similar and the alignment of $\widehat{\omega}_i(k_c^{(\omega)})$ to the stretching direction is most pronounced when $k_c^{(s)} \approx k_c^{(\omega)}/4$ irrespective of $k_c^{(\omega)}$ and the Reynolds number.

Looking again at Fig. 9, we notice that $G(k_c^{(s)} = 2k_c^{(\omega)},k_c^{(\omega)})$ is negative for $k_c^{(\omega)} > 4k_f$. This implies that vortices at a given scale in the inertial range are contracted by the strain at about half their scale. Such contraction may be observed in Fig. 3(b) (see also Fig. 13 in Sec. III E), where the red vortices are weakened in the region where yellow vortices are created probably because of the contraction in strain fields induced by the yellow vortices. In other words, the balance between the stretch in larger-scale strains and the contraction in the smaller-scale strains sustains the hierarchy. Detailed arguments, such as core dynamics analysis [44], are needed to examine this balance more quantitatively.

The above observation that vortices tend to be created by other vortices about twice as large as them is consistent with the classical view of the scale-by-scale energy cascade. However, Fig. 9 shows that the scale dependence of the vortex stretching is rather broad and even the contribution from the scale eight times as large is not negligible. Note in particular that the contribution of the strain directly driven by the external force ($k_c^{(s)} \approx k_f$) can nonlocally affect small-scale vortices.

This relatively broad (in scale) contribution to the stretching is the reason why the alignment between a vortex tube (for example, the blue vortices in Fig. 14 in Sec. III E) at a given length scale and larger-scale vortices seems random. Nevertheless, it can be verified that the strongly stretched vortices do align perpendicular to larger-scale intense vortices. The conditional PDF $\widetilde{P}(\cos\theta|r)$ of the cosine of the angle θ between two vortex axes at two different coarse-grained wave numbers $k_c^{(\mathrm{small})}$ and $k_c^{(\mathrm{large})}$ ($<k_c^{(\mathrm{small})}$) is plotted in Fig. 11 for three cases of $k_c^{(\mathrm{large})}$, where the turbulence with $\boldsymbol{f}^{(V)}$ is examined because the nonlocality of the stretching is most pronounced (Fig. 9) when the location of the external force is spatially fixed. The PDF $\widetilde{P}$ is conditional; that is, we only consider the angle between the smaller-scale vortex tubes stretched strongly enough [i.e., conditioned by the stretching rate $g(k_c^{(\mathrm{large})},k_c^{(\mathrm{small})})$ defined in (4)] and the larger-scale vortices of sufficient intensity [i.e., conditioned by the coarse-grained enstrophy $\widehat{Q}(k_c^{(\mathrm{large})})$]. It is not surprising from the observation in Fig. 3 that vortices at $k_c = 4k_f$ (yellow vortices in Fig. 3) tend to be perpendicular (i.e., $\theta = \pi/2$) to the largest-scale (red) vortices [the gray curve in Fig. 11(a)]. Because the lifetimes of the largest-scale vortices are much longer than those of the smaller-scale vortices, this perpendicular alignment to

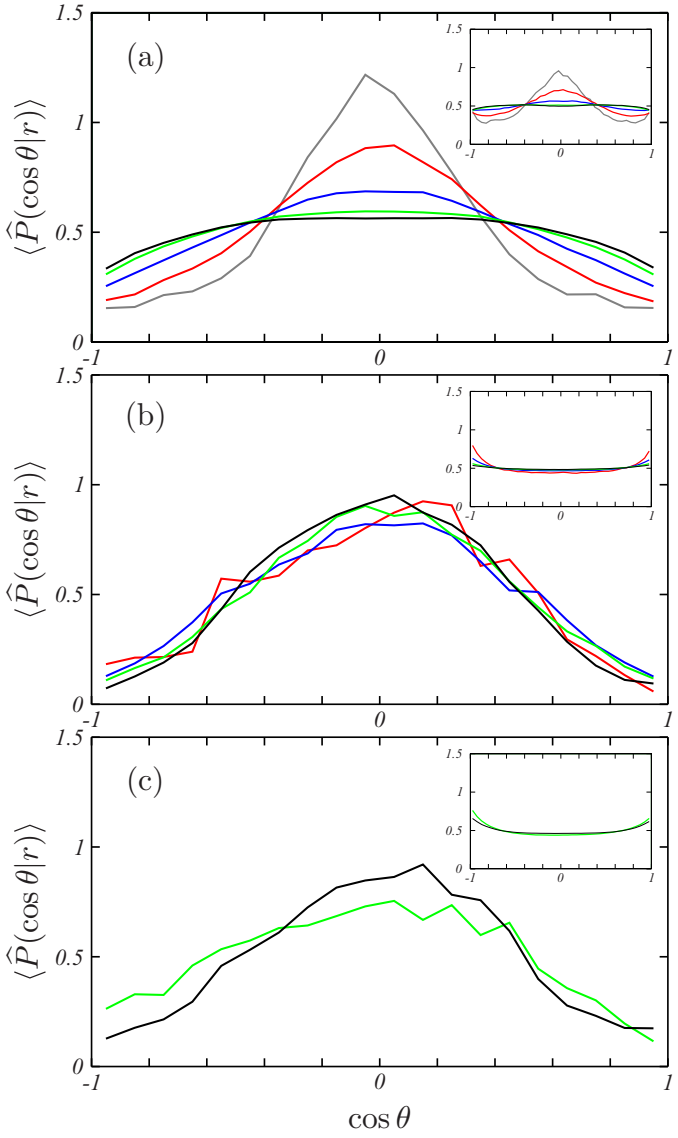

FIG. 11. Temporally averaged PDF of the cosine of the angle θ between the vortices at two different coarse-grained scales $k_c^{(\mathrm{small})}$ and $k_c^{(\mathrm{large})}$ ($<k_c^{(\mathrm{small})}$) with the distance r being $0.35\ell_c^{(\mathrm{large})} < r < 0.5\ell_c^{(\mathrm{large})}$. Different colors correspond to different coarse-grained scales for smaller vortices: gray, $k_c^{(\mathrm{small})} = 4k_f$; red, $8k_f$; blue, $16k_f$; green, $32k_f$; black, $64k_f$. The turbulence ($\langle R_\lambda\rangle = 480$) driven by $\boldsymbol{f}^{(V)}$ is examined. (a) $k_c^{(\mathrm{large})} = k_f$. The PDF is conditioned as the stretching rate $g(k_c^{(\mathrm{large})},k_c^{(\mathrm{small})}) > \langle\widehat{m}\rangle$ and the coarse-grained enstrophy $\widehat{Q}(k_c^{(\mathrm{large})}) > \langle\widehat{m}\rangle$. (b) $k_c^{(\mathrm{large})} = 4k_f$. The PDF is conditioned as $g(k_c^{(\mathrm{large})},k_c^{(\mathrm{small})}) > \langle\widehat{m}\rangle + 3\langle\widehat{\sigma}\rangle$ and $\widehat{Q}(k_c^{(\mathrm{large})}) > \langle\widehat{m}\rangle + 2\langle\widehat{\sigma}\rangle$. (c) $k_c^{(\mathrm{large})} = 16k_f$. The PDF is conditioned as $g(k_c^{(\mathrm{large})},k_c^{(\mathrm{small})}) > \langle\widehat{m}\rangle + 4\langle\widehat{\sigma}\rangle$ and $\widehat{Q}(k_c^{(\mathrm{large})}) > \langle\widehat{m}\rangle + 4\langle\widehat{\sigma}\rangle$. The insets show the PDF without conditions on the stretching rate g and the enstrophy $\widehat{Q}$.

the largest-scale vortices is also observed for smaller scales [Fig. 11(a)] and such an alignment to largest-scale vortices is observed even without the conditioning based on g and $\widehat{Q}$ [the inset of Fig. 11(a)]. Conversely, for smaller scales (i.e., larger $k_c^{(\mathrm{large})}$) angles between vortex tubes of different scales are distributed rather isotropically [the insets of Figs. 11(b) and 11(c)]. However, interestingly,

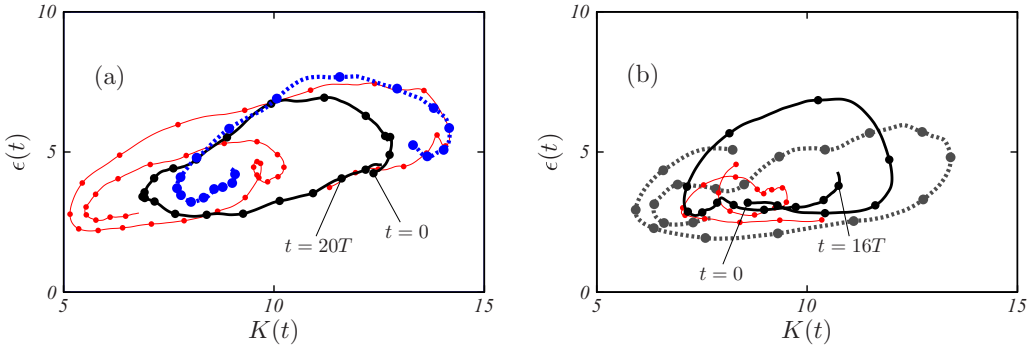

FIG. 12. (a) Temporal evolution of the kinetic energy $K(t)$ per unit mass and the dissipation rate $\epsilon(t)$ of the turbulence driven by the steady force $\boldsymbol{f}^{(V)}$. The evolution is counterclockwise. The interval between two successive dots indicates the turnover time $T = \langle L \rangle / \langle u' \rangle$ of the largest eddies. The Reynolds number $\langle R_\lambda \rangle = 280$ (thin red line), 480 (black solid line), and 750 (blue dotted line). (b) Same as (a) but for the turbulent Kolmogorov flow driven by $\boldsymbol{f}^{(K)}$. The Reynolds number $\langle R_\lambda \rangle = 190$ (gray dotted line), 310 (thin red line), and 490 (black solid line).

the perpendicular alignment ($\theta = \pi/2$) between smaller- and larger-scale vortex tubes is evident, when the PDF is conditioned on the stretching rate g of the smaller-scale (offspring) vortex tubes and the enstrophy $\widehat{Q}$ of the large-scale (parent) vortex tubes [Figs. 11(b) and 11(c)]. These results are consistent with the suggested picture of the sustaining mechanism of the hierarchy of vortex tubes, because antiparallel pairs of vortex tubes induce intense stretching in their perpendicular directions. Incidentally, the thresholds of g and $\widehat{Q}$ for the plots in Fig. 11 were chosen by trial and error to examine the anisotropic alignments because a vortex at given length scale is simultaneously stretched by vortices at various length scales (Fig. 9) and therefore the scale dependence of the thresholds is not trivial.

Thus the third conclusion of this paper is that vortices at each hierarchical level are most likely to be stretched in strain fields around 2–8 times larger vortices. If we assume that this vortex stretching leads to the cascade of energy to smaller scales, this conclusion supports the classical view of the scale-by-scale energy cascade. However, the somewhat broad contribution from larger-scale vortices makes the alignments between vortices at successive scales, in particular at small scales, rather obscure.

E. Quasiperiodic evolution

Since the energy at a given scale is possessed by vortex tubes at the same scale [30], the scale locality of vortex creation shown in the preceding section implies that it takes a finite time for the energy to cascade from the forcing scale to the dissipative scale. This finite-time energy cascade leads to an interesting phenomenon. Namely, even when turbulence is sustained by a steady force such as $\boldsymbol{f}^{(V)}$ and $\boldsymbol{f}^{(K)}$, it evolves quasiperiodically with significant temporal fluctuations. We plot the temporal evolution of the kinetic energy $K(t)$ per unit mass and its dissipation rate $\epsilon(t)$ in Fig. 12 for each of steady forces $\boldsymbol{f}^{(V)}$ and $\boldsymbol{f}^{(K)}$. Their temporal fluctuations are non-negligible. The evolution is quasiperiodic in the counterclockwise direction in these figures and its period is about $20T$ for $\boldsymbol{f}^{(V)}$ and about $10T$ for $\boldsymbol{f}^{(K)}$ irrespective of $\langle R_\lambda \rangle$. Here $T = \langle L \rangle / \langle u' \rangle$ is the turnover time of the largest-scale eddies. We emphasize that the observed quasiperiodic behavior is not transient, but lasts permanently. Since the enstrophy $Q(t)$ is equal to $\nu^{-1}\epsilon(t)$, the strong fluctuation of $\epsilon(t)$ indicates that the activity of small-scale vortices varies significantly in time. On the other hand, since $K(t)$ is determined by the circulation velocity of the largest-scale eddies, its large fluctuation indicates that the activity of the largest eddies also varies in time. Because the activity transfers from larger-scale eddies to those of smaller scales (see Fig. 15 below and Ref. [45] for more detailed analyses), the

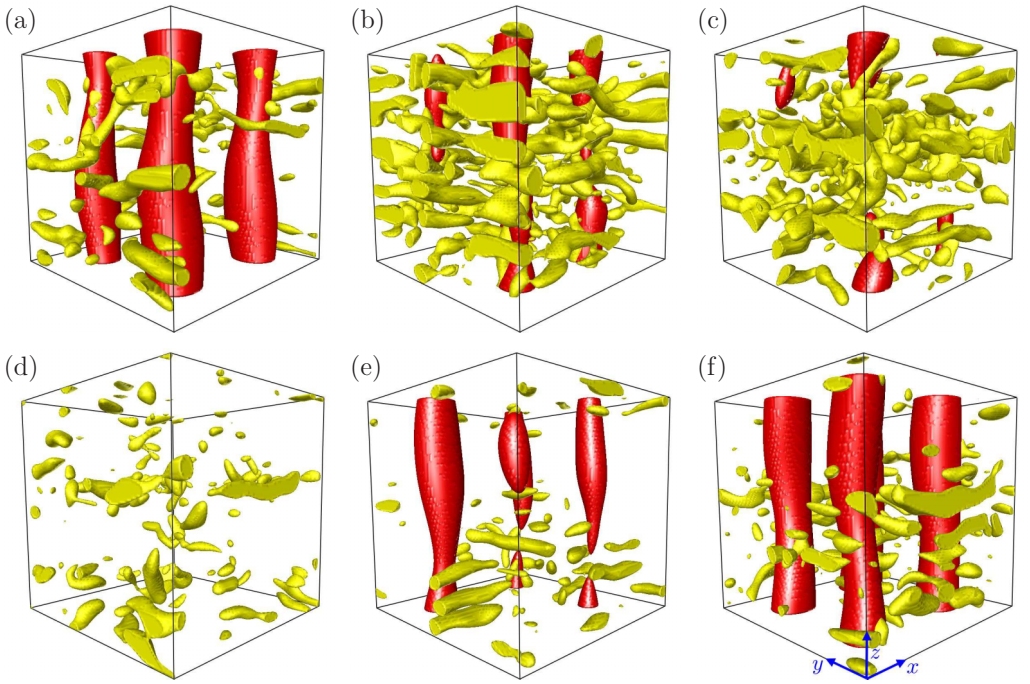

FIG. 13. Isosurfaces of coarse-grained enstrophy (red, $k_c = k_f$; yellow, $4k_f$) with threshold $\langle\widehat{m}\rangle + 2\langle\widehat{\sigma}\rangle$ in the turbulence driven by $\boldsymbol{f}^{(V)}$. The box size is $\mathcal{L}^3 \approx (5.4\langle L\rangle)^3 \approx (2200\langle\eta\rangle)^3$. Six snapshots on the black trajectory ($\langle R_\lambda\rangle = 480$) in Fig. 12(a) are shown at (a) $t = 0$, (b) $t = 4.4T$, (c) $t = 5.5T$, (d) $t = 11T$, (e) $t = 16T$, and (f) $t = 22T$.

phase of the evolution of $\epsilon(t)$ lags behind that of $K(t)$. This is the reason why the evolution becomes counterclockwise in Fig. 12. It is worth mentioning that quasiperiodic turbulence behavior driven by a time-independent force is observed in many flow systems. For example, significant temporal oscillations over 20 turnover times were experimentally observed by Pinton *et al.* [46] in the turbulent von Kármán flow.

The quasiperiodic behavior shown in Fig. 12 can be consistently explained in terms of the scale-by-scale energy cascade discussed in the previous sections. For this purpose, we plot quasicyclic evolution [along the black trajectory for $\langle R_\lambda\rangle = 480$ in Fig. 12(a)] of the isosurfaces of $\widehat{Q}$ for three different k_c in Figs. 13 and 14, where the coloring is the same as in Fig. 2, i.e., the red, yellow, and blue blobs are isosurfaces of $\widehat{Q}$ at $k_c = k_f$, $4k_f$, and $16k_f$, respectively. Here k_f is the forcing wave number, which corresponds to the length scale of $\ell_f = \mathcal{L}/k_f \approx 3.9\langle L\rangle \approx 1600\langle\eta\rangle$.

The temporal evolution (Figs. 13 and 14) of vortex tubes in the turbulence driven by $\boldsymbol{f}^{(V)}$ is summarized as follows. (i) Around the red vortex tubes created by $\boldsymbol{f}^{(V)}$, smaller-scale yellow vortices appear [Figs. 13(a)–13(c)] and then further smaller-scale blue vortex tubes are created around them [Fig. 14(b)]. (ii) Through this energy cascade to smaller scales, the large-scale red vortex tubes become quiescent [Figs. 13(c) and 13(d)]. Indeed, around the time [$t \approx 5T$; Figs. 13(c) and 14(b)] when the small-scale vortices are created, the energy dissipation rate attains its maximum [see Fig. 12(a)] and $K(t)$ drastically decreases afterward. (iii) Since $K(t)$ (i.e., the source of the energy cascade) is exhausted, the entire system consequently becomes quiescent [Figs. 13(d) and 14(c)]. (iv) When the activity at small scales declines, the energy input due to the force dominates and the red large-scale vortex tubes are reproduced [Figs. 13(e) and 13(f)]. Because of this cyclic behavior of strong vortex tubes, $K(t)$ and $\epsilon(t)$ evolve quasiperiodically [Fig. 12(a)].

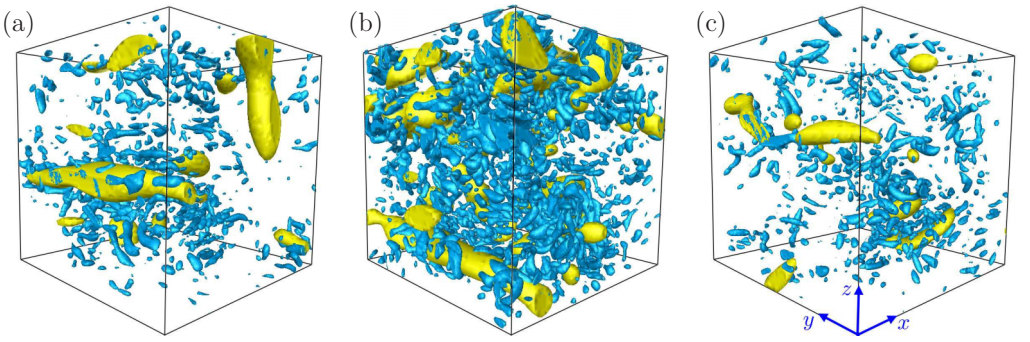

FIG. 14. Isosurfaces of coarse-grained enstrophy (yellow, $k_c = 4k_f$; blue, $k_c = 16k_f$) with threshold $\langle \widehat{m} \rangle + 2\langle \widehat{\sigma} \rangle$ in a $(1/2)^3$ part of Fig. 13 at (a) $t = 0$, (b) $t = 5.5T$, and (c) $t = 11T$.

To quantitatively verify that the quasiperiodic evolution of $K(t)$ and $\epsilon(t)$ is related to the successive creation of vortices at different length scales, we plot the temporal evolution of the spatial average of coarse-grained enstrophy at three different length scales by three thick dotted lines in Fig. 15(a). The values in the figure are normalized by the temporal average and standard deviation so that we can see the time lags between the activity of vortices at the different scales. It is evident that the smaller-scale activity lags behind the larger-scale one and the time lag becomes shorter for smaller scales. This is consistent with the picture that smaller-scale vortices are created by being stretched by 2–8 times larger-scale vortices (Sec. III D) because the strain rate is larger at smaller scales. The black thin line in Fig. 15(a) shows the energy input rate $\Pi(t)$, which evolves together with the activity of the largest-scale vortices. The energy dissipation rate $\epsilon(t)$, which evolves together with the smallest-scale vortices, therefore lags behind $\Pi(t)$ with the cascading time (that is about $5T$ in this case with the external force $\boldsymbol{f}^{(V)}$). This is the reason why $\Pi(t)$ and $\epsilon(t)$ evolve in the counterclockwise direction in Fig. 15(b), in which three curves for three different Reynolds numbers are plotted. The period of the cycles shown in Figs. 12(a) and 15(b) is approximately independent of the Reynolds number. This is also consistent with the picture that the cyclic behavior is caused by the scale-by-scale energy cascade.

Similarly, quasiperiodic evolution [Fig. 12(b)] of $K(t)$ and $\epsilon(t)$ of the turbulent Kolmogorov flow corresponds to cyclic behavior of the activity of vortices (Fig. 16). When a pair of red energetic vortex tubes is established [Fig. 16(b)], smaller-scale yellow vortex tubes are created perpendicular to them [Figs. 16(b) and 16(c)]. Accordingly, further smaller-scale vortex tubes are created (figure is not shown), the energy dissipation rate becomes large [see Fig. 12(b)], and the entire system becomes quiescent [Fig. 16(d)]. Afterward, the external force creates large-scale vortex tubes again [Fig. 16(e)]. Thus, in both cases with $\boldsymbol{f}^{(V)}$ and $\boldsymbol{f}^{(K)}$, such successive creations of vortices lead to the quasiperiodic behavior shown in Fig. 12.

It is also interesting to observe that despite the strong temporal fluctuations (Fig. 12) of $K(t)$ and $\epsilon(t)$ the statistics of the alignment between vortex tubes at a given length scale are steady. Evidence is given in the insets of Figs. 8(b) and 8(c), which show that the conditional PDF $P(\cos\theta|r)$ is surprisingly time independent. This contrasts with the fact that the strength of the vortices significantly depends on time (Fig. 12) and implies that a continuous energy transfer may be sustained by these background vortices. This result reinforces the conclusion in Sec. III C that not only conspicuously strong vortices, but also weaker background vortices tend to align in an antiparallel manner at each level of the hierarchy.

The fourth conclusion of this paper is that, because it takes a finite time to transfer the energy from the forcing scale to a dissipative scale due to the scale-by-scale creation of vortices, turbulence driven by a steady force evolves quasiperiodically.

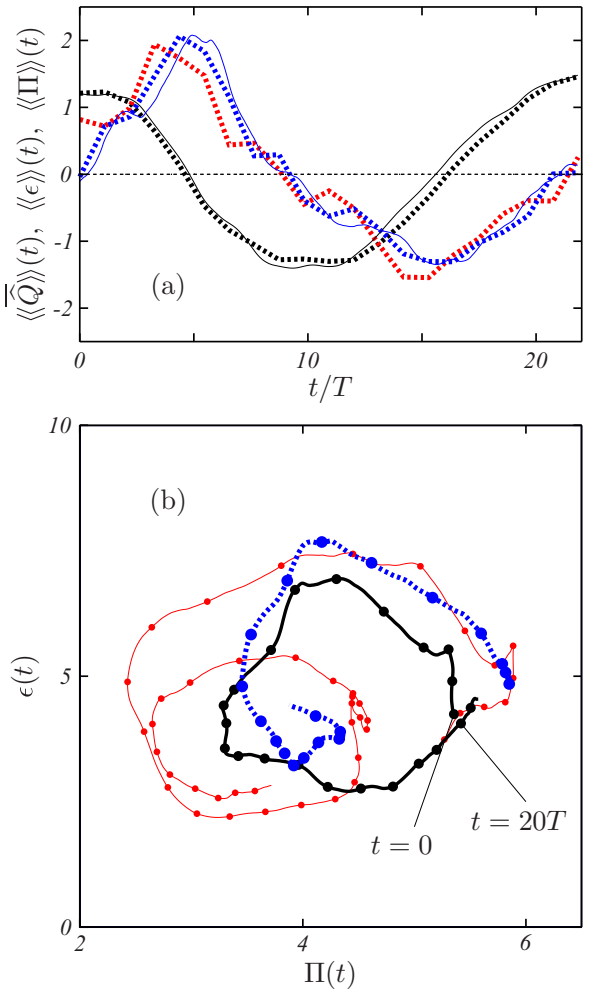

FIG. 15. (a) Time lags in the spatial average of the coarse-grained enstrophy $\widehat{Q}$ at three different length scales (black dotted line, $k_c = k_f$; red dotted line, $2k_f$; blue dotted line, $4k_f$), the energy input rate $\Pi(t)$ (black thin line), and the dissipation rate $\epsilon(t)$ (blue thin line) of the turbulence ($\langle R_\lambda\rangle = 480$) driven by $\boldsymbol{f}^{(V)}$. Brackets $\langle\langle\cdot\rangle\rangle$ denote the normalization by the temporal mean and standard deviation. (b) Cyclic evolution of $\Pi(t)$ and $\epsilon(t)$ of the turbulence driven by $\boldsymbol{f}^{(V)}$ at three different values of the Reynolds number. The Reynolds number $\langle R_\lambda\rangle = 280$ (thin red line), 480 (black solid line), and 750 (blue dotted line).

F. Generation process of antiparallel pairs of vortex tubes

Before closing the paper, we investigate the generation process of antiparallel pairs of vortex tubes in detail. Figure 17 shows the temporal evolution of vortices with a shorter time interval ($\approx 0.27T$) in a cropped region of Fig. 13. As demonstrated in this figure (see also Ref. [47]), the yellow vortex tubes in Fig. 13 hardly move from the beginning of their creation. In this region, there exists a large-scale straining field in the x direction in front of the red vortex tube shown in Fig. 17 (i.e., between the pair of red vortex tubes shown in Fig. 13). This is the reason why so many yellow (quarter-sized) vortex tubes parallel to the x direction are created. For example, let us look at the yellow antiparallel pair P_1 at time $t = 2.74T$. This pair grows together from $t \approx 2.2T$ and this process seems similar to the schematic in Fig. 14(b) of Ref. [18], drawn as a process of smaller-scale vortex creation around a single large vortex tube (see also Ref. [48] for an update of their view).

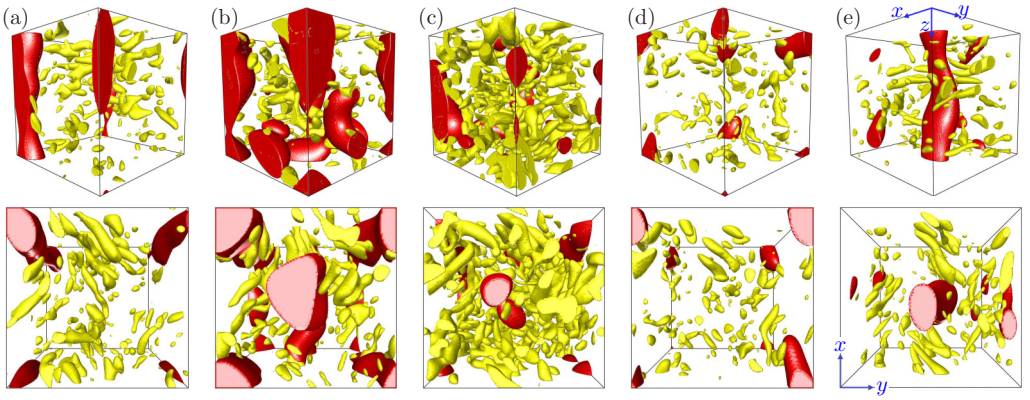

FIG. 16. Isosurfaces of coarse-grained enstrophy (red, $k_c = \sqrt{2}k_f$; yellow, $4\sqrt{2}k_f$) with threshold $\langle\widehat{m}\rangle + 2\langle\widehat{\sigma}\rangle$ in the turbulence driven by $\boldsymbol{f}^{(K)}$. The box size is $\mathcal{L}^3 \approx (4.2\langle L\rangle)^3 \approx (2200\langle\eta\rangle)^3$. Five snapshots on the black trajectory ($\langle R_\lambda\rangle = 490$) in Fig. 12(b) are shown at (a) $t = 0$, (b) $t = 3.3T$, (c) $t = 4.9T$, (d) $t = 7.4T$, and (e) $t = 11.5T$. Upper figures are side views and lower ones are top views.

Another example of the creation of yellow antiparallel vortex pairs (P_2 and P_3 at $t = 4.10T$) is the following: At $t \approx 3.3T$, a counterrotating vortex tube (V_2) emerges next to the vortex marked by V_1 and then at $t \approx 3.8T$ another vortex tube (which is counterrotating to V_2) is created to form P_3. Such successive creations of vortex tubes in the neighborhood of an intense vortex are frequently observed. These observations imply that several smaller-scale vortex tubes are stretched together

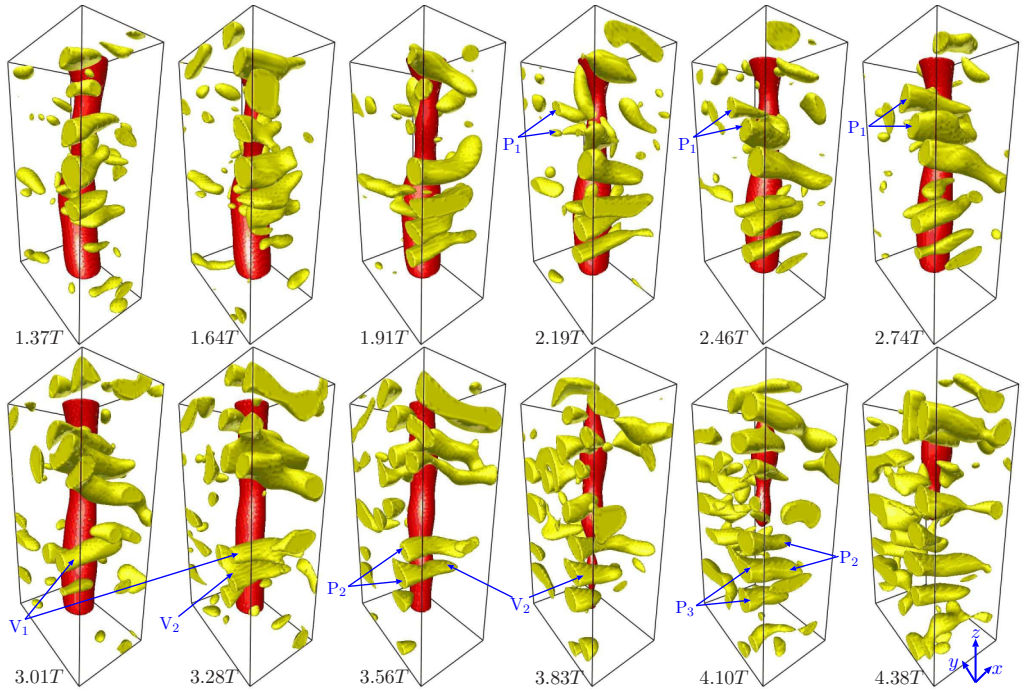

FIG. 17. Same as Fig. 13, but only a cropped region is shown with a shorter time interval ($0.27T$). A supplemental movie is also available in Ref. [47].

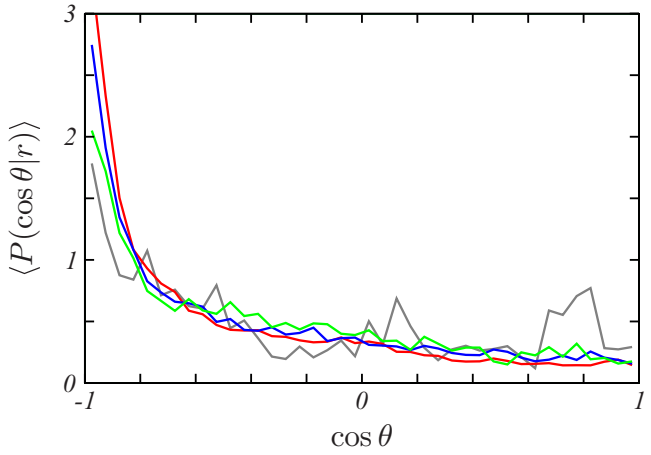

FIG. 18. Averaged PDF of the cosine of the angle θ between the axes of newly formed vortices and those surrounding them with the distance r being $0.5\ell_c < r < 0.75\ell_c$ for four different k_c. The results are for turbulence at $\langle R_\lambda \rangle = 200$ driven by $\boldsymbol{f}^{(V)}$. The same coloring is used as in Fig. 8(b) for $k_c = 4k_f$, $8k_f$, $16k_f$, and $32k_f$.

in a single larger-scale strain field. This is the main cause of the formation of antiparallel pairs of smaller vortex tubes. It is also evident in Fig. 17 that the lifetime of individual smaller-scale (yellow) vortices is too short for the self- and mutually induced advection observed in the collapse of vortex filaments [38] to form antiparallel pairs.

To quantitatively verify the observation that the vortex pairs are not formed by their approach to one another, we track the identified vortex axes backward in time to determine the time of their births. Then the PDF $P(\cos\theta|r)$ is evaluated between the newly formed vortex tubes and those surrounding them at a distance r at the time of their birth. The result is shown in Fig. 18, which is almost identical to the PDF in Fig. 8 for the angle θ between all vortices at various ages. This result is consistent with the above conclusion that antiparallel vortex tubes are formed from the beginning of their creation.

Thus the fifth conclusion of this paper is that vortex tubes created in larger-scale strain fields tend to form antiparallel pairs from their birth.

IV. CONCLUSION

Turbulence at sufficiently high Reynolds numbers in a periodic cube is composed of a self-similar hierarchy of antiparallel pairs of vortex tubes with various radii and lengths. It has been verified by visualizations (Figs. 3–5) and by statistical analyses (Fig. 8) that vortex tubes at a hierarchy level tend to form antiparallel (i.e., counterrotating) pairs. The distribution (Fig. 8) of angles between vortex axes is independent of the type of external forces. The hierarchy of vortex tubes is sustained by creation of smaller-scale vortices due to stretching in larger-scale strain fields. This sustaining mechanism of a hierarchy of vortices was predicted by previous authors (see, for example, Ref. [18]) and our DNSs have updated it. Since antiparallel pairs of vortices induce stronger strains than single vortices, larger-scale paired vortices more effectively create smaller-scale vortices around them (Figs. 3–5, 19, and 20). The sustaining mechanism of the hierarchy is also supported by our statistical analysis showing that strongly stretched vortex tubes tend to align in the direction perpendicular to larger-scale intense vortex tubes (Fig. 11). Concerning the generation mechanism of antiparallel pairs, visualizations (Fig. 17 and Ref. [47]) and statistical analyses (Fig. 18) show that vortex tubes at a given length scale form antiparallel pairs from their birth. This is because antiparallel pairs of smaller-scale vortex tubes are created together by a single larger-scale strain

under the constraint of angular momentum conservation. Although we could not identify a concrete mechanism of creation of antiparallel vortex pairs in our previous studies [30,31], the above results on the basis of the tracking of individual vortices show that Siggia's mechanism [38] is irrelevant for their formation. In other words, our prediction depicted in Fig. 6(a) of Ref. [31] is wrong. Instead, we have demonstrated in Fig. 17 that smaller-scale antiparallel pairs of vortices are created through a process similar to the schematic in Fig. 14(b) of Ref. [18], though the process is observed around paired, rather than single, vortices in our DNSs.

One of the most important conclusions of this paper is that strain fields at the scale twice as large as the stretched vortex is the strongest contributor to the stretching and creation of smaller-scale vortices, but even strain at the scale eight times as large can contribute (Fig. 9). This feature is also independent of the external forcing. The observed scale locality of the vortex stretching is consistent with the locality of energy transfer in wave-number space predicted using closure theories [49] and examined using DNSs [14–16]. Recall that the creation of smaller-scale vortices is related to energy transfer to smaller scales [27,30,31]. Indeed, we have verified that the observed intense cascade events cause energy transfer in wave-number space [45]. This scale-local energy cascade is the cause of another interesting phenomenon that the turbulence driven by the steady forces is not steady and that the activity of vortices at each hierarchy level evolves quasiperiodically (Fig. 12). In contrast, the angle distribution between the vortex axes is steady [insets of Figs. 8(b) and 8(c)]. This implies that, while weak background vortices sustain the mean energy cascade, the successive creation of strong vortices (Figs. 13, 14, and 16) leads to the significant temporal fluctuation.

A key concept in the present paper is the formation of antiparallel vortex tubes. The creation of antiparallel pairs of smaller vortex tubes perpendicular to larger vortices is frequently observed in various flow systems, for example, in mixing layers [50], in the wake behind a cylinder [51], and in the wake behind a flat plate [52]. Interestingly, Moisy and Jiménez [53] observed antiparallel spiraling structures of intense vortices, which seem to be located within a core of a large-scale vortex. The core dynamics [44,54,55], therefore, may be important also in the formation of antiparallel pairs of vortices, although we have paid attention only to strain fields outside of large-scale vortices (see also the Appendix). It is also worth mentioning that an antiparallel pair of orthogonal vortices (such as bridges) plays an essential role in vortex reconnections (see Ref. [56] and references therein) and Hussain and co-workers [17,54] suggested that vortex reconnections could lead to successive energy cascade from larger to smaller scales.

Thus we have successfully drawn a concrete picture of the hierarchy of antiparallel vortices in spatially periodic turbulence and explained its generation mechanism in terms of vortex stretching. However, there also remain some future works. First, it is not clear how the picture of a hierarchy of vortices and the mechanism of energy cascade are related to the Kolmogorov scaling in the inertial range. Second, although we have carefully examined the suggested picture of the hierarchy, we cannot fully exclude other possibilities because the picture may depend on the coarse-grain and identification method of coherent vortices. Recalling that details of the shape of the smallest-scale vortices depend on numerical resolutions [43], the shape of coarse-grained vortices can depend on filtering methods. Although in our analysis we have not observed structures similar to Lundgren's spiral [19], Horiuti and Fujisawa [21] reported spiral structures in spatially periodic turbulence, though at lower Reynolds numbers, by using a different identification method of coherent vortices. It would therefore be interesting to compare their method with ours in higher-Reynolds-number turbulence. Third, we have not developed arguments on the instability of the elements of the hierarchy of vortices. We have shown that smaller-scale vortices are created by being stretched in strain fields around larger-scale vortices. It is therefore reasonable to assume that the time scale of the creation of these smaller-scale vortices is proportional to the reciprocal of the strain rate at the larger scale. To complete the scenario of the energy cascade, we need to show that the time scale of the decay of larger-scale vortices is longer, at least in the prefactor, than that of the creation of smaller-scale vortices. Although our flow visualizations suggest that this is indeed the case, we need to identify the instability and estimate its growth rate for more quantitative arguments. Such a theoretical investigation is likely to lead to deeper understanding of the dynamics and statistics of

the energy cascade and may give us useful information on the first problem mentioned above. For this purpose, the circulation of vortices is essential because it controls their instability. It is therefore an important future study to estimate circulations of individual vortices at each level of hierarchy by extending our technique of the identification of scale-by-scale vortex axes. Fourth, although we have restricted ourselves to the case of spatially periodic turbulence sustained by an external force, an important avenue of future study would be to examine the universality of the observed hierarchy in various turbulent flows. In particular, it is interesting to examine whether or not the hierarchy observed in the forced turbulence is altered in decaying turbulence in a periodic cube. Another immediate target may be the wall-bounded turbulence (see a review by Jiménez [57]), since it is possible to conduct DNS of turbulence in a channel, for example, at sufficiently high Reynolds numbers to be accompanied by both the power-law energy spectrum and the logarithmic-law mean flow velocity.

ACKNOWLEDGMENTS

This work was partly supported by JSPS Grants-in-Aid for Scientific Research No. 25249014, No. 26630054, and No. 16H04268. The DNSs were conducted with the support and under the auspices of the NIFS Collaboration Research programs (NIFS13KNSS043 and NIFS15KNSS066).

APPENDIX: CLUSTER OF WORMLIKE VORTICES

Figure 1 shows that the isosurfaces of enstrophy exist intermittently in space and they form clusters. Similar clusters of the wormlike vortices are observed at much higher Reynolds numbers [58]. One might imagine that the clusters of the smallest-scale vortices correspond to larger-scale

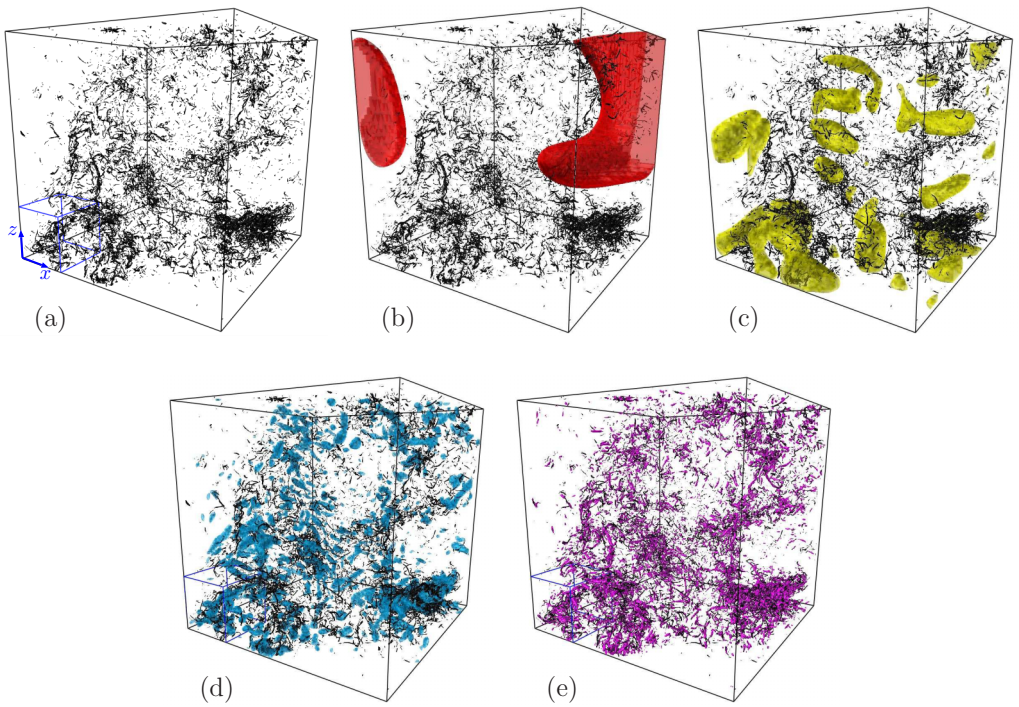

FIG. 19. Black objects are isosurfaces of enstrophy in the turbulence ($\langle R_\lambda \rangle = 390$) driven by $\boldsymbol{f}^{(R)}$. (a) Same as Fig. 1 but from another line of sight. (b)–(e) Colored objects are isosurfaces of enstrophy coarse grained at (b) $k_c = k_f$ (threshold is $\langle \widehat{m} \rangle + 2\langle \widehat{\sigma} \rangle$), (c) $k_c = 4k_f$ ($\langle \widehat{m} \rangle + 2\langle \widehat{\sigma} \rangle$), (d) $k_c = 16k_f$ ($\langle \widehat{m} \rangle + 3\langle \widehat{\sigma} \rangle$), and (e) $k_c = 64k_f$ ($\langle \widehat{m} \rangle + 5\langle \widehat{\sigma} \rangle$). The size of the shown cube is $(\mathcal{L}/2)^3 \approx (3.5\langle L \rangle)^3 \approx (1500\langle \eta \rangle)^3$.

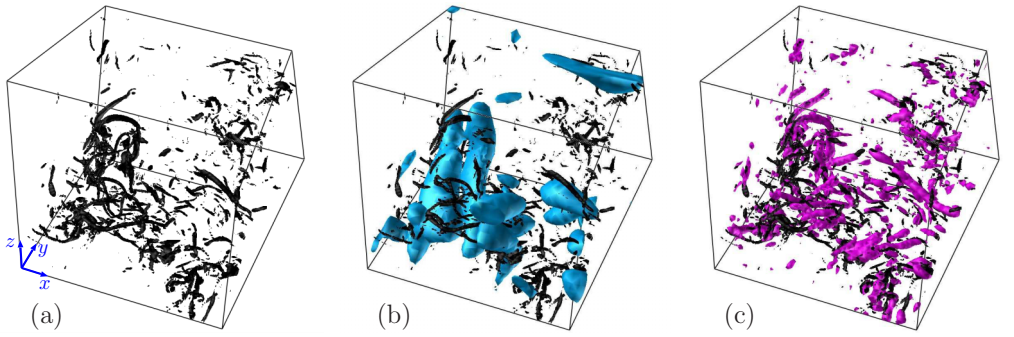

FIG. 20. Magnified views of a cropped region (shown with the blue frame) in Figs. 19(a), 19(d), and 19(e), respectively. The size of the shown cube is $(\mathcal{L}/8)^3$.

vortices and such multiple-scale clusters of the smallest-scale vortices compose a hierarchy of multiple-scale vortices. However, this seems not to be the case. As was recognized by several authors [30,33], a larger-scale vortex is not necessarily composed of a cluster of wormlike vortices. In this Appendix we show evidence of this in the case of the turbulence driven by $\boldsymbol{f}^{(R)}$, but the shown results are independent of the kind of the external force.

Figure 19(a) is another view of Fig. 1(a). There are voids of the wormlike vortices in the left upper and right upper regions in this figure. As shown in Fig. 19(b), where we plot isosurfaces (red blobs) of the enstrophy coarse-grained at $k_c = k_f$, the largest-scale vortices exist in these voids (rather than clusters) of the wormlike vortices. Furthermore, it is evident in Fig. 19(c) that yellow vortices at the scale $k_c = 4k_f$, which corresponds to a quarter of the scale of the red vortices, are also in the void regions of the black isosurfaces of the enstrophy.

We plot in Figs. 19(d) and 19(e) smaller-scale vortices. The purple blobs in Fig. 19(e) are isosurfaces of the coarse-grained enstrophy at $k_c = 64k_f$. This figure and its magnified view, Fig. 20(c), show that purple vortices coincide well with wormlike vortices [Figs. 19(a) and 20(a)]. This is reasonable because $k_c = 64k_f$ corresponds to the length scale $17\langle\eta\rangle$, which is approximately the smallest length scale in this turbulence. Figure 19(d) shows the vortices at an intermediate length scale between yellow ones in Fig. 19(c) and purple ones in Fig. 19(e). In this global view [Fig. 19(d)], blue vortices at $k_c = 16k_f$ exist in the regions where the wormlike vortices also exist. However, we see in a magnified view [Fig. 20(a)] that a considerable number of black vortices are located around blue larger vortices. For example, in the left region of Fig. 20(b), there is a pair vortex tubes, which are counterrotating, and black vortices exist along the direction of the stretching around the pair. This observation is consistent with the mechanism of vortex creations described in the main text (see Sec. III B). Incidentally, we also observe the cases that a few black vortices are located within a blue vortex. Although similar observations that a larger vortex seems to be composed of a cluster of a few wormlike structures were reported by previous authors [53], the majority of smaller-scale vortices exist around larger-scale vortices, the hierarchy cannot be a nested structure of vortices.

To summarize this Appendix, the hierarchy of vortices in the inertial range is not composed of clusters of the wormlike vortices. Large-scale vortices exist in their voids rather than in their clusters.

[1] L. F. Richardson, Atmospheric diffusion shown on a distance-neighbour graph, Proc. R. Soc. London Ser. A **110**, 709 (1926).

[2] L. F. Richardson, *Weather Prediction by Numerical Process* (Cambridge University Press, Cambridge, 1922).

[3] A. N. Kolmogorov, The local structure of turbulence in incompressible viscous fluid for very large Reynolds numbers, Dokl. Akad. Nauk SSSR **30**, 301 (1941) [Proc. R. Soc. London A **434**, 9 (1991)].
[4] Y. Tsuji and B. Dhruva, Intermittency feature of shear stress fluctuation in high-Reynolds-number turbulence, Phys. Fluids **11**, 3017 (1999).
[5] A. N. Kolmogorov, A refinement of previous hypotheses concerning the local structure of turbulence in a viscous incompressible fluid at high Reynolds number, J. Fluid Mech. **13**, 82 (1962).
[6] U. Frisch, P. L. Sulem, and M. Nelkin, A simple dynamical model of intermittent fully developed turbulence, J. Fluid Mech. **87**, 719 (1978).
[7] R. Benzi, G. Paladin, G. Parisi, and A. Vulpiani, On the multifractal nature of fully developed turbulence and chaotic systems, J. Phys. A **17**, 3521 (1984).
[8] Z. She and E. Leveque, Universal Scaling Laws in Fully Developed Turbulence, Phys. Rev. Lett. **72**, 336 (1994).
[9] U. Frisch, *Turbulence, The Legacy of A. N. Kolmogorov* (Cambridge University Press, Cambridge, 1995).
[10] E. D. Siggia, Numerical study of small-scale intermittency in three-dimensional turbulence, J. Fluid Mech. **107**, 375 (1981).
[11] R. M. Kerr, Higher-order derivative correlations and the alignment of small-scale structures in isotropic numerical turbulence, J. Fluid Mech. **153**, 31 (1985).
[12] K. Yamamoto and I. Hosokawa, A decaying isotropic turbulence pursued by the spectral method, J. Phys. Soc. Jpn. **57**, 1532 (1988).
[13] A. Vincent and M. Meneguzzi, The dynamics of vorticity tubes in homogeneous turbulence, J. Fluid Mech. **258**, 245 (1994).
[14] R. M. Kerr, Velocity, scalar and transfer spectra in numerical turbulence, J. Fluid Mech. **211**, 309 (1990).
[15] J. A. Domaradzki and R. S. Rogallo, Local energy transfer and nonlocal interactions in homogeneous, isotropic turbulence, Phys. Fluids A **2**, 413 (1990).
[16] K. Ohkitani and S. Kida, Triad interactions in a forced turbulence, Phys. Fluids A **4**, 794 (1992).
[17] A. K. M. F. Hussain, Coherent structures and turbulence, J. Fluid Mech. **173**, 303 (1986).
[18] M. V. Melander and F. Hussain, Coupling between a coherent structure and fine-scale turbulence, Phys. Rev. E **48**, 2669 (1993).
[19] T. S. Lundgren, Strained spiral vortex model for turbulent fine structure, Phys. Fluids **25**, 2193 (1982).
[20] A. D. Gilbert, A cascade interpretation of Lundgren's stretched spiral vortex model for turbulent fine structure, Phys. of Fluids A **5**, 2831 (1993).
[21] K. Horiuti and T. Fujisawa, The multi-mode stretched spiral vortex in homogeneous isotropic turbulence, J. Fluid Mech. **595**, 341 (2008).
[22] K. Horiuti and T. Ozawa, Multimode stretched spiral vortex and nonequilibrium energy spectrum in homogeneous turbulence, Phys. Fluids **23**, 035107 (2011).
[23] R. M. Kerr, Swirling, turbulent vortex rings formed from a chain reaction of reconnection events, Phys. Fluids **25**, 065101 (2013).
[24] S. A. Orszag and G. S. Patterson, Numerical Simulation of Three-Dimensional Homogeneous Isotropic Turbulence, Phys. Rev. Lett. **28**, 76 (1972).
[25] Y. Kaneda, T. Ishihara, M. Yokokawa, K. Itakura, and A. Uno, Energy dissipation rate and energy spectrum in high resolution direct numerical simulations of turbulence in a periodic box, Phys. Fluids **15**, L21 (2003).
[26] P. E. Dimotakis, The mixing transition in turbulent flows, J. Fluid Mech. **409**, 69 (2000).
[27] H. Tennekes and J. L. Lumley, *A First Course in Turbulence* (MIT Press, Cambridge, 1972).
[28] A. Tsinober, *An Informal Introduction to Turbulence* (Kluwer, Dordrecht, 2001).
[29] P. A. Davidson, *Turbulence—An Introduction for Scientists and Engineers* (Oxford University Press, Oxford, 2004).
[30] S. Goto, A physical mechanism of the energy cascade in homogeneous isotropic turbulence, J. Fluid Mech. **605**, 355 (2008).
[31] S. Goto, Coherent structures and energy cascade in homogeneous turbulence, Prog. Theor. Phys. Suppl. **195**, 139 (2012).
[32] M. Farge, Wavelet transforms and their applications to turbulence, Annu. Rev. Fluid Mech. **24**, 395 (1992).

[33] T. Leung, N. Swaminathan, and P. A. Davidson, Geometry and interaction of structures in homogeneous isotropic turbulence, J. Fluid Mech. **710**, 453 (2012).
[34] J. Jiménez, A. A. Wray, P. G. Saffman, and R. S. Rogallo, The structure of intense vorticity in isotropic turbulence, J. Fluid Mech. **255**, 65 (1993).
[35] J. Jeong and F. Hussain, On the identification of a vortex, J. Fluid Mech. **285**, 69 (1995).
[36] H. Miura and S. Kida, Identification of tubular vortices in turbulence, J. Phys. Soc. Jpn. **66**, 1331 (1997).
[37] S. Kida and H. Miura, Swirl condition in low-pressure vortex, J. Phys. Soc. Jpn. **67**, 2166 (1998).
[38] E. D. Siggia, Collapse and amplification of a vortex filament, Phys. Fluids **28**, 794 (1985).
[39] A. M. Obukhov, Kolmogorov flow and laboratory simulation of it, Russ. Math. Surv. **38**, 113 (1983).
[40] V. Borue and S. A. Orszag, Numerical study of three-dimensional Kolmogorov flow at high Reynolds numbers, J. Fluid Mech. **306**, 293 (1996).
[41] M. E. Brachet, D. I. Meiron, S. A. Orszag, B. G. Nickel, R. H. Morf, and U. Frisch, Small-scale structure of the Taylor-Green vortex, J. Fluid Mech. **130**, 411 (1983).
[42] K. Horiuti and Y. Takagi, Identification method for vortex sheet structures in turbulent flows, Phys. Fluids **17**, 121703 (2005).
[43] I. Bermejo-Moreno, D. I. Pullin, and K. Horiuti, Geometry of enstrophy and dissipation, grid resolution effects and proximity issues in turbulence, J. Fluid Mech. **620**, 121 (2009).
[44] M. V. Melander and F. Hussain, Core dynamics on a vortex column, Fluid Dyn. Res. **13**, 1 (1994).
[45] T. Yasuda, S. Goto, and G. Kawahara, Quasi-cyclic evolution of turbulence driven by a steady force in a periodic cube, Fluid Dyn. Res. **46**, 061413 (2014).
[46] J.-F. Pinton, P. C. W. Holdsworth, and R. Labbé, Power fluctuations in a closed turbulent shear flow, Phys. Rev. E **60**, R2452 (1999).
[47] See Supplemental Material at http://link.aps.org/supplemental/10.1103/PhysRevFluids.2.064603 for a movie.
[48] F. Hussain, D. S. Pradeep, and E. Stout, Nonlinear transient growth in a vortex column, J. Fluid Mech. **682**, 304 (2011).
[49] R. H. Kraichnan, Inertial-range transfer in two- and three-dimensional turbulence, J. Fluid Mech. **47**, 525 (1971).
[50] L. P. Bernal and A. Roshko, Streamwise vortex structure in plane mixing layers, J. Fluid Mech **170**, 499 (1986).
[51] C. H. K. Williamson, Vortex dynamics in the cylinder wake, Annu. Rev. Fluid. Mech. **28**, 477 (1996).
[52] F. M. Najjar and S. Balachandar, Low-frequency unsteadiness in the wake of a normal flat plate, J. Fluid Mech. **370**, 101 (1998).
[53] F. Moisy and J. Jiménez, Geometry and clustering of intense structures in isotropic turbulence, J. Fluid Mech. **513**, 111 (2004).
[54] D. S. Pradeep and F. Hussain, Core dynamics of a strained vortex: instability and transition, J. Fluid Mech. **447**, 247 (2001).
[55] D. S. Pradeep and F. Hussain, Vortex dynamics of turbulence coherent structure interaction, Theor. Comput. Fluid Dyn. **24**, 265 (2010).
[56] S. Kida and M. Takaoka, Vortex reconnection, Annu. Rev. Fluid. Mech. **26**, 169 (1994).
[57] J. Jiménez, Cascades in wall-bounded turbulence, Annu. Rev. Fluid Mech. **44**, 27 (2012).
[58] T. Ishihara, Y. Kaneda, and J. C. R. Hunt, Thin shear layers in high Reynolds number turbulence DNS results, Flow, Turbul. Combust. **91**, 895 (2013).